

# Differentially Coherent Multichannel Detection of Acoustic OFDM Signals

Yashar M. Aval, *Student Member, IEEE*, and Milica Stojanovic, *Fellow, IEEE*

**Abstract**—In this paper, we propose a class of methods for compensating for the Doppler distortions of the underwater acoustic channel for differentially coherent detection of orthogonal frequency-division multiplexing (OFDM) signals. These methods are based on multiple fast Fourier transform (FFT) demodulation, and are implemented as partial (P), shaped (S), fractional (F), and Taylor (T) series expansion FFT demodulation. They replace the conventional FFT demodulation with a few FFTs and a combiner. The input to each FFT is a specific transformation of the input signal, and the combiner performs weighted summation of the FFT outputs. The four methods differ in the choice of the pre-FFT transformation (P, S, F, T), while the rest of the receiver remains identical across these methods. We design an adaptive algorithm of stochastic gradient type to learn the combiner weights for differentially coherent detection. The algorithm is cast into the multichannel framework to take advantage of spatial diversity. The receiver is also equipped with an improved synchronization technique for estimating the dominant Doppler shift and resampling the signal before demodulation. An additional technique of carrier sliding is introduced to aid in the post-FFT combining process when residual Doppler shift is nonnegligible. Synthetic data, as well as experimental data from a recent mobile acoustic communication experiment (few kilometers in shallow water, 10.5–15.5-kHz band) are used to demonstrate the performance of the proposed methods, showing significant improvement over conventional detection techniques with or without intercarrier interference equalization (5–7 dB on average over multiple hours), as well as improved bandwidth efficiency [ability to support up to 2048 quadrature phase-shift keying (QPSK) modulated carriers].

**Index Terms**—Differentially coherent detection, Doppler, fading, intercarrier interference (ICI) mitigation, orthogonal frequency-division multiplexing (OFDM), stochastic gradient algorithm, synchronization, underwater acoustic communication.

## I. INTRODUCTION

THE main challenge for coherent detection of signals over underwater acoustic (UWA) channels is accurate channel estimation. Factors contributing to this challenge include the long delay spread, time variation of the UWA channel, and the

wideband nature of the transmitted signals. This fact motivates differentially coherent detection as a low complexity alternative which does not require explicit channel estimation. Unlike with single-carrier broadband modulation, where equalization would have to be juggled with differentially coherent detection, orthogonal frequency-division multiplexing (OFDM) easily lends itself to differentially coherent detection, since each of the carriers conveys only a narrowband signal.

OFDM has been extensively studied for UWA channels, with almost all of the published work focusing on coherent detection. Various methods for coherent detection have been proposed which address single-transmitter [1]–[4] or multiple-transmitter system configurations [5]–[7], and channels with mild or more severe Doppler distortion that require dedicated intercarrier interference (ICI) equalization (e.g., [1] and [3]). Channel estimation is typically accomplished using pilots only [1], [7], or decision feedback instead or in addition to pilots [4], [5]. Channel estimation algorithms that have been considered range from standard least squares type [5] to more sophisticated ones that involve a basis or matching pursuit to take advantage of the sparse nature of the channel [3], [4].

In contrast to coherent detection, differentially coherent detection does not require channel estimation, relying instead on channel invariance either between adjacent carriers (differential encoding in frequency) or between adjacent OFDM blocks (differential encoding in time). If there is perfect channel knowledge, differential detection comes at some penalty in the performance; however, in cases where time variation prevents accurate channel estimation, performance of coherent detection degrades accordingly, and differential detection becomes competitive or even superior to coherent detection. This fact has been observed in both wireless radio channels [8] and, more recently, in UWA channels [9].

In this paper, we consider differential encoding in frequency as it supports our design goal of increasing bandwidth efficiency. Bandwidth efficiency is defined as the ratio of symbol rate to bandwidth  $R/B$ , which is proportional to  $1/(1 + T_g B/K)$ , where  $T_g$  is the guard interval between OFDM blocks, at least equal to the multipath spread, and  $K$  is the number of carriers. As the number of carriers increases in a given bandwidth, both the bandwidth efficiency and the coherence between carriers increase (due to smaller carrier spacing  $\Delta f = B/K$ ) thus making differential encoding in frequency a natural choice.

The number of carriers, however, cannot grow indefinitely due to the channel variation (see Fig. 1). As the number of carriers within a given bandwidth grows, the length of the OFDM block  $T = 1/\Delta f$  increases, nudging the coherence time of the

Manuscript received August 18, 2013; revised February 07, 2014 and March 05, 2014; accepted May 28, 2014. Date of publication June 20, 2014; date of current version April 10, 2015. This work was supported in part by the U.S. Office of Naval Research (ONR) under Grants N00014-07-1-0738 and N00014-09-1-0700; and by the National Science Foundation (NSF) under Grant CNS-1212999.

Associate Editor: S. Zhou.

The authors are with the Electrical and Computer Engineering Department, Northeastern University, Boston, MA 02115 USA (e-mail: aval.y@husky.neu.edu; millitsa@ece.neu.edu).

Color versions of one or more of the figures in this paper are available online at <http://ieeexplore.ieee.org>.

Digital Object Identifier 10.1109/JOE.2014.2328411

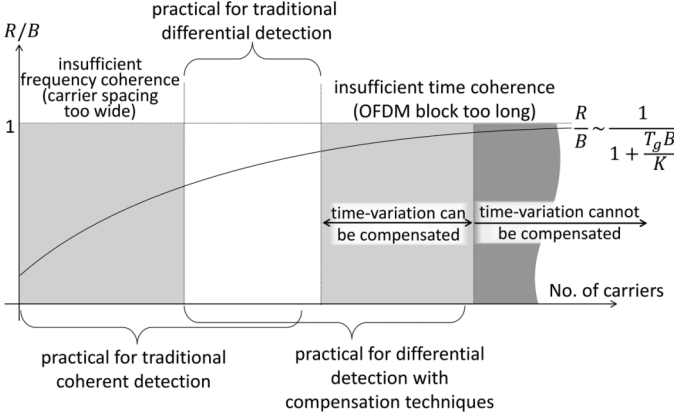


Fig. 1. Relationship between the number of carriers and bandwidth efficiency.

channel. In such a case, orthogonality between the carriers is lost, and the resulting ICI dominates the detection error for both coherent and differentially coherent detections.

Multiple approaches to ICI mitigation have been tested for coherent detection of acoustic OFDM signals, e.g., [2], [3], and [6]. These methods concentrate on post-fast-Fourier-transform (post-FFT) processing to alleviate ICI. In doing so, however, some of the useful information is lost during FFT demodulation [10]. Guided by this idea, we take a different approach that provides the receiver with access to some of the pre-FFT information. We couple this approach with differentially coherent detection to reduce the complexity and the burden of full channel estimation.

We propose four ICI mitigation methods: partial FFT demodulation (P-FFT), shaped FFT demodulation (S-FFT), fractional FFT demodulation (F-FFT), and Taylor expansion FFT demodulation (T-FFT). The idea of partial FFT demodulation was introduced to differential detection in [11] and for coherent detection using a single element receiver in [10]. However, neither of these references provided experimental data results. P-FFT demodulation was extended to a multichannel framework in [12] which contains both simulation and experimental results. Finally, F-FFT was introduced in [9].

Here, we present channel-matched filtering as a general idea, and propose the notion of the optimal receiver as a combination of channel-matched filtering and ICI equalization. We formulate P-FFT and F-FFT demodulation techniques as low-complexity approximations to channel-matched filtering, and also introduce two new techniques (S-FFT and T-FFT). Finally, we present extensive experimental results that demonstrate the performance of the techniques proposed.

The multiple-FFT demodulation techniques draw on the notion that the channel variations may be decomposed based on a set of predefined functions. Given such a decomposition, the received signal is projected onto these functions, and the projections are passed on to FFT demodulation and subsequent combining.

P-FFT uses decomposition onto a set of nonoverlapping flat windows in time, while S-FFT uses smooth windowing. F-FFT is based on a decomposition onto complex exponentials, and T-FFT uses Taylor series polynomials.

To arrive at the optimal combiner weights without having *a priori* knowledge of the channel, we employ an adaptive algo-

rithm. The adaptive algorithm may be designed either for coherent or differentially coherent detection. Here, we focus on differentially coherent detection and exploit the concept introduced in [11] which outlines a stochastic gradient algorithm for computing the combiner weights. Specifically, we extend this concept to different decomposition functions used for multiple-FFT demodulation, and cast it into the multielement receiver configuration by employing differential maximum ratio combining (D-MRC). Multielement processing is often necessary in practical acoustic systems as it offers spatial diversity needed to provide sufficient signal-to-noise ratio (SNR) for data detection.

A novel synchronization technique is introduced to enhance the accuracy of estimating the delay and dilation/compression factor necessary for resampling. To deal with the residual Doppler (after initial resampling), an additional method of sliding carriers is introduced to compensate for Doppler shifts that are greater than half the carrier spacing. Finally, the original gradient algorithm [12] is altered to introduce normalization which improves the convergence and provides robustness to spectral nulls.

We provide a detailed experimental analysis of the proposed ICI mitigation and array combining methods through simulation and experimental data, including the estimated probability distribution of the mean squared error (MSE) values and the achievable block error rates (BLERs). The experimental results are obtained from the 2010 Mobile Acoustic Communications Experiment (MACE'10) which was designed to challenge the performance of high-rate acoustic communications, where bandwidth-efficient OFDM signals are especially vulnerable to motion-induced Doppler effects.

The paper is organized as follows. We describe the system model in Section II. In Section III, we discuss optimal detection of OFDM signals over time-varying channels and propose four Doppler compensation methods as approximations to the optimal receiver. Differentially coherent receiver is presented in Section IV, and its performance is analyzed through simulation in Section V. Section VI contains the results of experimental data processing. Conclusions are summarized in Section VII.

## II. SYSTEM MODEL

The transmitted OFDM block with  $K$  carriers is given by

$$s(t) = \text{Re} \left\{ \sum_{k=0}^{K-1} d_k e^{j2\pi f_k t} \right\}, \quad t \in [0, T] \quad (1)$$

where  $T = 1/\Delta f$  is the block duration and  $d_k$  is the data symbol transmitted on the  $k$ th carrier of frequency  $f_k = f_0 + k\Delta f$ . The data symbols  $d_k$  belong to a unit-amplitude phase-shift keying (PSK) alphabet, and are differentially encoded in the frequency domain, such that  $d_k = d_{k-1}b_k$ ,  $k = 1, \dots, K-1$ , where  $b_k$  is the original PSK data symbol, and  $d_0$  is set to 1.

The signal received on the  $m$ th receiving element is modeled as

$$r_m(t) = \sum_p h_{p,m}(t) s(t - \tau_{p,m}(t)) + n_m(t), \quad m = 1, \dots, M \quad (2)$$

where the summation is taken over multiple propagation paths, represented by the gains  $h_{p,m}(t)$  and delays  $\tau_{p,m}(t)$ . The noise  $n_m(t)$  is assumed to be independent between the receiving elements.

After frame synchronization, initial resampling, down-shifting by the lowest carrier frequency  $f_0$ , and cyclic prefix (CP) removal, the received signal is modeled as<sup>1</sup>

$$v_m(t) = \sum_k H_k^m(t) d_k e^{j2\pi k \Delta f t} + w_m(t), \quad t \in [0, T] \quad (3)$$

where  $H_k^m(t) = \sum_p h_{p,m}(t) e^{-j2\pi f_k \tau_{p,m}(t)}$  represents the channel coefficient and  $w_m(t)$  is the equivalent noise.

In a conventional OFDM system, the path gains and delays are practically constant over the block duration  $T$ , and so are the channel coefficients  $H_k^m(t) \approx H_k^m$ . However, this may not be the case in acoustic systems that are prone to motion-induced Doppler shifting and time-varying path gains. In particular, the path delays are often modeled as  $\tau_{p,m}(t) = \tau_{p,m} + a_{p,m}t$ , where  $a_{p,m}$  is the Doppler factor associated with the  $p$ th path and the  $m$ th receiving element [6]. Moreover, the path gains may as well exhibit an inherent slow variation that is of no particular form but is instead often regarded as random.

### III. OPTIMAL DETECTION OF OFDM SIGNALS OVER TIME-VARYING CHANNELS

In a conventional system, the received signal is subject to FFT demodulation which effectively yields<sup>2</sup>

$$y_k^m = \int_0^T v_m(t) e^{-j2\pi k \Delta f t} dt, \quad m = 1, \dots, M. \quad (4)$$

If the channel variation during one OFDM block is insignificant (i.e.,  $\tau_{p,m}(t) \approx \tau_{p,m}$  and  $h_{p,m}(t) \approx h_{p,m}$ ) the FFT outputs are modeled as

$$y_k^m = T H_k^m d_k + z_k^m \quad (5)$$

where the channel coefficient  $H_k^m = \sum_p h_{p,m} e^{-j2\pi f_k \tau_{p,m}}$  is considered to be time invariant during one OFDM block, and  $z_k^m$  is the noise.

When the channel is time varying, the post-FFT observations (4) no longer represent sufficient statistics for data detection. An optimal receiver can now be formulated based on the maximum-likelihood (ML) principle. Conditioned on observing the signal (3) only on the interval  $[0, T]$ , and assuming white Gaussian noise,<sup>3</sup> the ML detection rule is simply stated as

$$\tilde{\mathbf{d}} = \min_{\mathbf{d}} \sum_{m=1}^M \int_0^T |v_m(t) - \bar{v}_m(t)|^2 dt \quad (6)$$

<sup>1</sup>For zero-padded OFDM, CP removal is approximated by overlap adding [13] and an equivalent channel coefficient is defined accordingly.

<sup>2</sup>We will keep the notation with continuous time to simplify later treatment.

<sup>3</sup>Modeling the noise as white Gaussian is only needed to illustrate the concepts of optimal detection in a simple manner, and extension to nonwhite noise is straightforward. In practice, neither the channel nor the noise statistics are known *a priori*, and adaptive receivers are employed which do not make any assumption about the noise.

where

$$\bar{v}_m(t) = \sum_{k=0}^{K-1} H_k^m(t) d_k e^{j2\pi k \Delta f t} \quad (7)$$

and  $\mathbf{d} = [d_0, \dots, d_{K-1}]^T$ . Considering a single-element receiver, (6) implies a front-end processing that yields the (conditionally) sufficient statistics as<sup>4</sup>

$$v_k = \int_0^T v(t) H_k^*(t) e^{-j2\pi k \Delta f t} dt. \quad (8)$$

The signals  $v_k$  can also be expressed as

$$v_k = \sum_{l=0}^{K-1} R_v(k, l) d_l + w_k \quad (9)$$

where

$$R_v(k, l) = \int_0^T H_l(t) H_k^*(t) e^{j2\pi(l-k)\Delta f t} dt. \quad (10)$$

Expressed in vector form, the signals (9) are give by

$$\mathbf{v} = \mathbf{R}_v \mathbf{d} + \mathbf{w} \quad (11)$$

where the circularly symmetric, zero-mean, complex Gaussian noise  $\mathbf{w}$  has covariance  $2N_0 \mathbf{R}_v$  if the input noise is of power spectral density  $N_0$ . The optimal linear minimum mean-square (MMSE) receiver yields the data symbol estimates

$$\hat{\mathbf{d}}_v = \mathbf{Q}_v^H \mathbf{v} \quad (12)$$

where

$$\mathbf{Q}_v = (\mathbf{R}_v + 2N_0 \mathbf{I})^{-1} \quad (13)$$

and  $(\cdot)^H$  denotes conjugate transpose.

Thus, the optimal receiver consists of two steps: channel-matched filtering (8) and equalization (12). The resulting MMSE is

$$E_v = \frac{1}{K} E \left\{ \|\hat{\mathbf{d}}_v - \mathbf{d}\|^2 \right\} = 1 - \frac{\text{tr} [\mathbf{R}_v^H \mathbf{Q}_v]}{K} \quad (14)$$

where  $\text{tr}[\cdot]$  denotes the trace of a matrix.

In a system with a large number of carriers (e.g., 1024) even if the time-varying channel coefficients  $H_k(t)$  were known, individual channel-matched filtering would demand excessive computation. Therefore, the more common approach is to implement a suboptimal receiver with conventional front-end which avoids channel-matched filtering and employs low-complexity single-FFT demodulation. The outputs of the FFT demodulator in this case can be modeled as

$$y_k = \sum_{l=0}^{K-1} R_y(k, l) d_l + z_k \quad (15)$$

<sup>4</sup>These statistics are sufficiently conditioned on the fact that the received signal is truncated to the interval  $[0, T]$  after removing the guard interval. Such truncation caters to the use of same size FFT as in the time-invariant case, which in turn leads to computationally efficient receiver implementation.

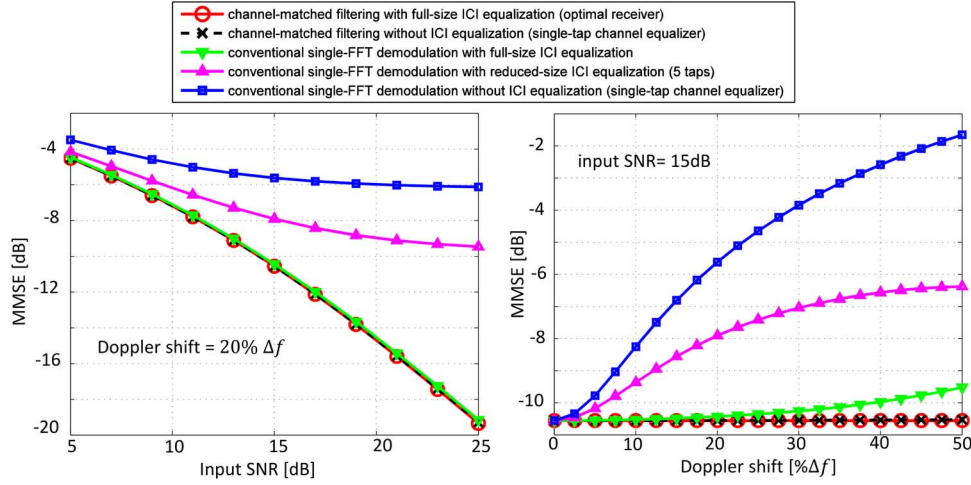


Fig. 2. MMSE performance with and without channel-matched filtering for varying size of the ICI equalizer. The channel consists of two paths with amplitudes 0.8 and 0.6, and a total delay spread of  $6T/K$ . The paths exhibit Doppler scaling at  $0.2\Delta f/f_0$  (MMSE versus SNR plot), or a varying Doppler (MMSE versus Doppler plot). These results show that channel-matched filtering enables the system to operate with a single-tap equalizer with practically no loss in performance in this example.

where

$$R_y(k, l) = \int_0^T H_l(t) e^{j2\pi(l-k)\Delta f t} dt. \quad (16)$$

Expressing (15) in vector form, we have

$$\mathbf{y} = \mathbf{R}_y \mathbf{d} + \mathbf{z} \quad (17)$$

where  $\mathbf{z}$  is circularly symmetric, zero-mean, complex Gaussian noise of covariance  $2N_0 T \mathbf{I}$ .

Linear MMSE ICI equalization now yields the data symbol estimates

$$\hat{\mathbf{d}}_y = \mathbf{Q}_y^H \mathbf{y} \quad (18)$$

where

$$\mathbf{Q}_y = (\mathbf{R}_y \mathbf{R}_y^H + 2N_0 T \mathbf{I})^{-1} \mathbf{R}_y \quad (19)$$

and the corresponding MMSE is

$$E_y = \frac{1}{K} E \left\{ \|\hat{\mathbf{d}}_y - \mathbf{d}\|^2 \right\} = 1 - \frac{\text{tr}[\mathbf{R}_y^H \mathbf{Q}_y]}{K}. \quad (20)$$

Further reduction in computational complexity is often achieved by replacing the full-size equalizer with a short one (a few taps per carrier instead of all  $K$ ). This approach is justified by the fact that the matrix  $R_y$  typically has a banded structure, with fast-decaying off-diagonal elements [3]. The idea is equally applicable to the conventional system operating on the signals  $y_k$  and to the system operating on the matched-filter outputs  $v_k$ . Details of these schemes and the resulting MMSE metrics are provided in the Appendix.

In evaluating the various approaches (with/without channel-matched filtering, with full/short/no ICI equalizer),<sup>5</sup> the following questions arise: 1) How much is gained by using channel-matched filtering as compared to conventional, single-FFT demodulation? 2) How sensitive is each system to

<sup>5</sup>We use the term “no ICI equalization” to describe the case with a single-tap channel equalizer.

equalizer shortening? To answer these questions, Fig. 2 shows the MMSE achieved by the two systems (with and without matched filtering) in configurations with a varying size ICI equalizer. The channel used to generate this example is a two-path channel whose time variation is a consequence of motion-induced Doppler shifting. Shown in the two plots are the theoretical values of the MMSE versus SNR for a fixed Doppler shift, and MMSE versus the Doppler shift for a fixed SNR. The Doppler shift is evaluated for the lowest carrier frequency  $f_0$  and expressed as a percentage of the carrier spacing  $\Delta f$ . Given that  $E\{|d_k|^2\} = 1$ , the input SNR for QPSK symbols is defined as  $\text{SNR} = T \sum_p |h_p|^2 / 2N_0$ .

Comparing the performance of the two systems in configuration with full-size ICI equalization (the number of taps equal to the number of carriers), we note that matched filtering does not gain much on this channel over the conventional system. However, as the equalizer is shortened, conventional demodulator shows a significant loss in performance. With a five-tap equalizer, in a high-SNR regime (SNR = 20 dB) there is about 5 dB of loss at 20%  $\Delta f$  Doppler shift. Without ICI equalization, the conventional system is completely challenged in the presence of anything but a negligible Doppler scaling. In contrast, the system with channel-matched filtering retains near-optimal performance even with a single-tap equalizer. This fact serves as a strong motivation for using front-end filtering, as it indicates that the outputs of the channel-matched filters contain little residual ICI.

#### A. Channel Decomposition

To arrive at a computationally efficient method of applying channel-matched filtering, let us suppose that the channel coefficients  $H_k^m(t)$  admit a decomposition onto a set of known functions  $\phi_i(t)$ , such that

$$H_k^m(t) \approx \sum_{i=0}^{I-1} H_{k,i}^m \phi_i(t). \quad (21)$$

If such a decomposition can be established, (8) can equivalently be represented as

$$v_k^m \approx \sum_{i=0}^{I-1} H_{k,i}^{m*} y_{k,i}^m \quad (22)$$

where

$$y_{k,i}^m = \int_0^T \phi_i^*(t) v_m(t) e^{-j2\pi k \Delta f t} dt. \quad (23)$$

In practice,  $y_{k,i}^m, k = 0, \dots, K-1$ , can be obtained as the outputs of an FFT operation applied to the input  $v_m(t)\phi_i^*(t)$ . There are  $I$  such inputs formed using the known functions  $\phi_i(t)$ , and, hence,  $I$  FFTs are required to approximate channel-matched filtering. Since the channel coefficients  $H_k^m(t)$  typically vary slowly over time,  $I$  can be small, making the resulting receiver computationally efficient.

Some choices of the functions  $\phi_i(t)$  will be better suited than others to a particular channel distortion, in which case a smaller value of  $I$  would suffice. We employ four types of such functions: nonoverlapping rectangular windows in time spanning the block interval  $T$ , overlapping raised cosine windows, complex exponentials, and polynomials of the Taylor series type. We call the corresponding multiple-FFT demodulation methods P-FFT, S-FFT, F-FFT, and T-FFT demodulation, respectively. Specifically, the functions  $\phi_i(t)$  for these four choices are given by

$$\phi_i(t) = \begin{cases} \text{rect}\left(\frac{It}{T} - i\right) & \text{P-FFT} \\ \frac{\text{rect}\left(\frac{(I-1)t}{2T} - \frac{i-1}{2}\right) \left(1 + \cos\left(\frac{(I-1)\pi t}{T} - i\pi\right)\right)}{2} & \text{S-FFT} \\ e^{j2\pi i \frac{\Delta f}{T} t} & \text{F-FFT} \\ c_0^{(i)} + c_1^{(i)}t + \dots + c_{i-1}^{(i)}t^{i-1} & \text{T-FFT} \end{cases} \quad (24)$$

where  $i = 0, \dots, I-1$ ,  $t \in [0, T]$ , and  $\text{rect}(x)$  is a unit-amplitude rectangular pulse, covering the interval  $x \in [0, 1]$ . The Taylor polynomials include all powers of  $t$  up to the highest, with coefficients that are chosen so as to make the functions  $\phi_i(t)$  orthogonal. We will comment on this choice later in this section. These choices of  $\phi_i(t)$  are visualized in Fig. 3.

P-FFT divides the received OFDM block into  $I$  sections which are  $I$  times shorter than the original OFDM block. If the sections are sufficiently short, the channel variations are expected to be negligible during each section. The combiner reassembles the sections after giving each section a different weight. P-FFT thus resembles channel-matched filtering where the function  $H_k^{m*}(t)$  is approximated as piecewise constant.

While P-FFT was shown to be effective in compensating for the channel variations [10], [12], the precision of the approximation can be improved by smoothing the transitions between the sections. To this end, we introduce S-FFT which provides a smooth decomposition of the channel, preserving the continuity of the approximations to  $H_k^{m*}(t)$ . This change, however, comes at the cost of correlation between FFT outputs as the sections have some overlap. Correlation reduces the convergence

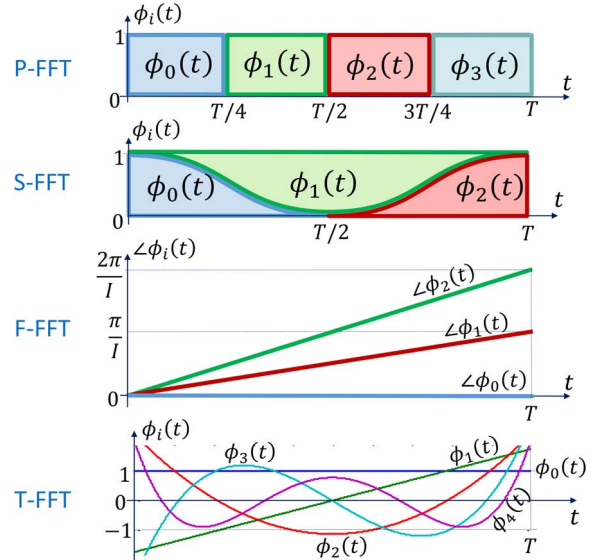


Fig. 3. Four candidate choices for  $\phi_i(t)$ : nonoverlapping rectangular waveforms, each covering an interval of length  $T/I$  (P-FFT), raised-cosine waveforms (S-FFT), complex exponentials at multiples of a fraction of the carrier spacing  $\Delta f/I$  (F-FFT), and orthogonal polynomials of degrees 0 to  $I-1$  (T-FFT).

speed of the adaptive stochastic gradient algorithm that will be employed for learning the optimal combiner weights,<sup>6</sup> but the results will show that the effect of discontinuity of P-FFT decomposition is more detrimental to the performance than the effect of limited correlation.

F-FFT provides frequency-domain samples of the received signal at fractions of the carrier spacing to make it easier for the receiver to compensate for the large Doppler shifts [9]. Sampling the spectrum at half the carrier spacing ( $I = 2$ ) makes compensation of any Doppler shift in the range  $[-\Delta f/2, \Delta f/2]$  feasible at very low complexity (a three-tap combiner suffices). Frequency-domain oversampling was originally introduced to UWA communication in [14], where the channel is estimated through a set of pilot carriers which are distributed over the bandwidth as equally spaced. Each pilot is isolated by two null carriers to enable ICI-free estimation of the channel and the Doppler spread. The estimates are then employed to detect each set of three payload carriers using nine frequency samples, spaced by half the carrier spacing. The current work differs in that it does not allocate pilots or null carriers (except for a few pilots at the beginning of a frame), and operates in decision-directed mode.

T-FFT is based on polynomial expansion of the time-varying channel coefficients. The idea of estimating the channel coefficients  $H_k^m(t)$  in time and/or frequency domain by polynomials was also introduced in [15] and used for equalization in [16], where a 2-D polynomial expansion (in time and frequency) is employed to increase the accuracy of channel estimation and ICI equalization. While Wang *et al.* [16] use the time-domain polynomial approximation to compute the equalizer taps, we employ this approximation to overcome the channel variations in the time domain by applying channel-matched filtering, followed by equalization (if desired) to remove the remaining ICI.

<sup>6</sup>This reduction in speed of convergence is due to separation of eigenvalues.



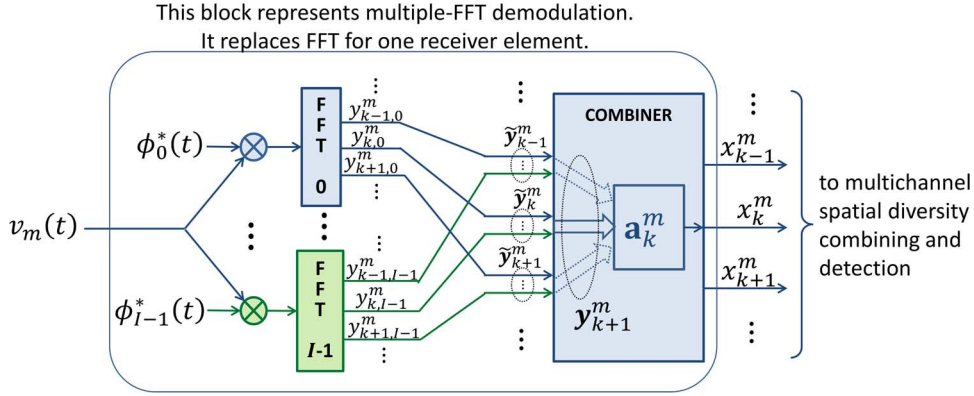


Fig. 4. Block diagram of multiple-FFT demodulation with P-FFT, S-FFT, F-FFT, or T-FFT. The choice of the functions  $\phi_i(t)$  determines which of the four methods is applied. If ICI equalization is desired, the combiner inputs are extended to include the FFT outputs from the neighboring carriers (dashed arrows inside the combiner block). The goal of multiple-FFT demodulation and combining is to reduce the ICI in the outputs  $x_k^m$ .

Wang *et al.* [16] also define an approximation similar to Taylor series (i.e.,  $\phi_i(t) = (t - (T/2))^i$ ), while we use the set of coefficients  $c_0^{(i)}, c_1^{(i)}, \dots, c_{i-1}^{(i)}$  as a degree of freedom to construct the polynomials  $\phi_i(t)$  that are orthogonal to one another on the interval  $t \in [0, T]$ . Orthogonalization is accomplished via the Gram–Schmidt procedure. Using orthogonal polynomials minimizes correlation between the inputs to the combiner and, therefore, increases the convergence speed of the adaptive algorithm.

### B. Combiner

According to (22), the outputs of the FFTs for any of the methods should be weighted in proportion to the channel ( $H_{k,i}^*$ ) and summed before being fed to the equalizer (12) to suppress the remaining ICI. When the channel is not known, estimates of the channel coefficients are needed to implement the two steps of channel-matched filtering and equalization. An alternative that overcomes the complexity of such an approach is to treat the two steps jointly, since together they represent a single linear transformation of the input signal. A combiner whose weights are determined adaptively can then be implemented. Specifically, let us denote the vector of combiner weights corresponding to the  $k$ th carrier and the  $m$ th receiving element by  $\mathbf{a}_k^m$ , and let us define the corresponding input signal vector as

$$\mathbf{y}_k^m = [\dots |y_{k-1,0}^m \dots y_{k-1,I-1}^m | y_{k,0}^m \dots y_{k,I-1}^m | y_{k+1,0}^m \dots y_{k+1,I-1}^m | \dots]^T. \quad (25)$$

The combiner output is then given by

$$x_k^m = \mathbf{a}_k^{mH} \mathbf{y}_k^m. \quad (26)$$

The length of each combiner vector is  $L \geq I$ , and a particular choice of  $(I, L)$  specifies the receiver structure. For  $I = 1$ , this structure reduces to the conventional one with a single-FFT demodulator and an equalizer of size  $L$ , while for  $L = I$ , it corresponds to a single-tap equalizer. In general,  $L$  can be an integer multiple of  $I$ , but this is not necessary. For instance, if F-FFT is used with  $I = 2$ , one could choose  $\mathbf{y}_k^m = [y_{k-1,1}^m \ y_{k,0}^m \ y_{k,1}^m]^T$ , so that the combiner operates on the nominal demodulator output  $y_{k,0}^m$  and two adjacent components shifted by  $\pm \Delta f/2$ . In this case, the combiner is of length  $L = 3$ .

Fig. 4 shows the block diagram of multiple-FFT demodulation followed by the combiner.

If coherent detection is employed, the combiner outputs (26) are used directly to form the decision variable  $\hat{d}_k = \sum_m x_k^m$ . Spatial diversity is exploited in this case by determining the weight vectors  $\mathbf{a}_k^m$  so as to minimize the MSE in data detection, thus achieving the effect of MRC.<sup>7</sup>

### IV. DIFFERENTIALLY COHERENT DETECTION

Differentially coherent detection eases the burden on accurate channel tracking by exploiting the coherence between adjacent carriers. On a time-invariant channel with a single-element receiver, where  $H_k \approx H_{k-1}$ , the decision variable is simply formed from the single-FFT outputs as  $\hat{b}_k = y_k / y_{k-1}$ . In the case of spatial diversity with D-MRC, it is given by  $\hat{b}_k = \sum_m y_{k-1}^{*m} y_k^m / \sum_m |y_{k-1}^m|^2$ .

When the channel is time varying, narrow carrier spacing makes the OFDM signal vulnerable to Doppler distortion, ICI appears, and this simple detection method no longer applies. To overcome this seemingly aggravating problem, we capitalize on the principles of adaptive combining. Specifically, using a set of combiner weights  $\mathbf{a}_k^m$ , we form the preconditioned signals  $x_k^m$ , and use these signals to form the decision variable as

$$\hat{b}_k = \sum_m x_{k-1}^{m*} x_k^m = \mathbf{x}_{k-1}^H \mathbf{x}_k \quad (27)$$

where  $\mathbf{x}_k = [x_k^1 \ x_k^2 \ \dots \ x_k^M]^T$ . This decision variable represents the soft estimate of the transmitted symbol  $b_k$ , and the final decision  $\tilde{b}_k$  is made by choosing the closest point in the signal space. The combiner weights  $\mathbf{a}_k^m$  are determined so as to minimize the MSE in data detection, thus accounting for D-MRC. Note that these weights may differ substantially from the ones used in coherent detection. In particular, they are expected to change much more slowly across carriers, as differentially coherent detection is guided mostly by the phase difference between  $x_{k-1}^m$  and  $x_k^m$  and not directly by their values. The

<sup>7</sup>The term “combining” is used both to describe combining of multiple-FFT outputs and multichannel combining of spatially distinct receiving elements. The context is hopefully clear enough to distinguish between the two.

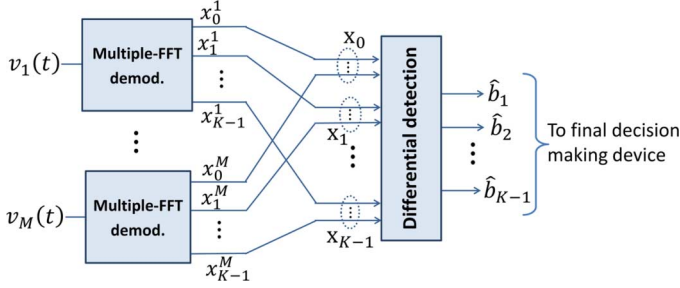


Fig. 5. Block diagram of differential detection with multiple-FFT demodulation. Each demodulator is as shown in Fig. 4. D-MRC is performed according to (27), and the combiner weight vectors  $\mathbf{a}_k^m$  are determined so as to minimize the MSE in data detection.

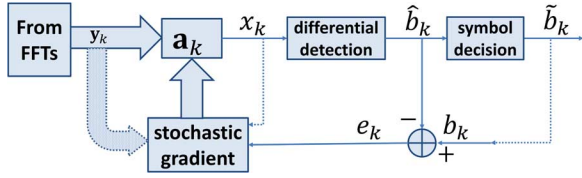


Fig. 6. Block diagram of the adaptive stochastic gradient method.

block diagram of the differentially coherent receiver is shown in Fig. 5.

#### A. Adaptive Algorithm

To arrive at the weights  $\mathbf{a}_k^m$  without the *a priori* knowledge of the channel, we define auxiliary variables  $\hat{b}_k^m = x_k^m / x_{k-1}^m$  and use the corresponding errors  $e_k^m = b_k - \hat{b}_k^m$  to formulate the MMSE solution for the individual weight vectors  $\mathbf{a}_k^m$ . Specifically, treating the adjacent coefficients  $\mathbf{a}_{k-1}^m$  and  $\mathbf{a}_k^m$  as being the same,<sup>8</sup> we arrive at the error gradient

$$\begin{aligned} \mathbf{g}_k^m &= - \frac{\partial \{ |e_k^m|^2 \}}{\partial \mathbf{a}_k^{m*}} \\ &= \frac{[\mathbf{y}_k^m x_{k-1}^m - \mathbf{y}_{k-1}^m x_k^m] e_k^{m*}}{(x_{k-1}^m)^2}. \end{aligned} \quad (28)$$

During training, the data symbols  $b_k$  needed to form the error  $e_k^m$  are known. Thereafter, the system is switched into decision-directed mode, where symbol decisions are made on the composite estimate (27). Note that this estimate is formed after multichannel combining. In this manner, the spatial diversity gain is exploited in obtaining the individual weight vectors. In practice, if long data streams are being transmitted, additional pilots can be inserted periodically to prevent error propagation.

The gradient (28) can be used directly to compute the combiner weights. However, a scaled gradient is advantageous for channels with high-frequency selectivity, where the channel response varies significantly across the signal bandwidth. On carriers whose strength is low (near spectral nulls), the original stochastic gradient algorithm suffers from noise enhancement due to the presence of the term  $(x_{k-1}^m)^2$  in the denominator. Furthermore, the error  $e_k^m$  is typically larger for the weak carriers, making the adaptive algorithm sensitive to these carriers. An

ideal algorithm should slow the learning process down when passing through spectral notches to prevent noise enhancement and possible loss of tracking. Therefore, we define the scaled gradient as

$$\bar{\mathbf{g}}_k^m = |x_{k-1}^m| \mathbf{g}_k^m \quad (29)$$

and employ a stochastic gradient algorithm to compute the combiner weights recursively as

$$\mathbf{a}_{k+1}^m = \mathbf{a}_k^m + \mu \bar{\mathbf{g}}_k^m \quad (30)$$

where  $\mu$  is a prespecified step size.

To further increase the robustness and guard against error propagation, we apply a thresholding method which prevents the combiner weights from changing if either the error  $e_k = b_k - \hat{b}_k$  or the gradient  $\mathbf{g}_k^m$  exceeds a predefined level. Such thresholding prevents abrupt changes to combiner weights which are likely to occur upon decision errors. The algorithm is summarized in Algorithm 1, and its block diagram is shown in Fig. 6. The algorithm is also available online [17].

---

#### Algorithm 1: Adaptive algorithm

---

```

Initialize  $\mathbf{a}_0^m$  and  $\mathbf{a}_1^m$  (see Table I)
set threshold_ek, threshold_gkm and  $\mu$ 
 $x_0^m = \mathbf{a}_0^{mH} \mathbf{y}_0^m, m = 1, \dots, M$ 
dir = +1
current_cycle = 1 : K - 1
next_cycle = K - 2 : -1 : 0
while for all OFDM blocks in one frame do
    for k = current_cycle do
         $x_k^m = \mathbf{a}_k^{mH} \mathbf{y}_k^m, m = 1, \dots, M$ 
         $\hat{b}_k = \sum_m x_{k-\text{dir}}^m x_k^m$ 
        if pilots available then
             $b_k = \text{pilot symbol}$ 
        else
             $b_k = \text{decision}\{b_k\}$ 
        end if
        for m = 1 : M do
             $e_k^m = \tilde{b}_k - (x_k^m / (x_{k-\text{dir}}^m))$ 
             $\mathbf{g}_k^m = ([\mathbf{y}_k^m x_{k-\text{dir}}^m - \mathbf{y}_{k-\text{dir}}^m x_k^m] e_k^{m*}) / (x_{k-1}^m)^2$ 
            if  $|b_k - \hat{b}_k| < \text{threshold\_ek} \ \& \ \mathbf{g}_k^m \mathbf{g}_k^m < \text{threshold\_gkm}$  then
                 $\mathbf{a}_{k+\text{dir}}^m = \mathbf{a}_k^m + \mu |x_{k-\text{dir}}^m| \mathbf{g}_k^m$ 
            end if
        end for
    end for
    save  $b_k$  and  $\hat{b}_k$ 
    load  $\mathbf{y}_k^m$  corresponding to the next OFDM block
    swap (current_cycle, next_cycle)
    dir = -dir
     $x_k^m = \mathbf{a}_k^{mH} \mathbf{y}_k^m, m = 1, \dots, M$ 
end while

```

---

Other algorithms may also be employed for learning the combiner weights. For example, the recursive least squares (RLS)

<sup>8</sup>This assumption is based on the fact that the channel frequency response does not change much from one carrier to the next.

TABLE I  
TYPICAL PARAMETERS OF THE FOUR PROPOSED METHODS

method	$I$	$L$	$\phi_0(t)$	$\phi_1(t)$	$\phi_2(t)$	initialization ( $\mathbf{a}_0^m$ )
P-FFT	2	6	$\text{rect}(2t/T)$	$\text{rect}(2t/T - 1)$	-	$[0 \ 0 \ 1 \ 1 \ 0 \ 0]^T$
S-FFT	2	6	$(1 + \cos(\pi t/T))/2$	$(1 - \cos(\pi t/T))/2$	-	$[0 \ 0 \ 1 \ 1 \ 0 \ 0]^T$
F-FFT	2	3	1	$e^{j2\pi\Delta f t/2}$	-	$[0 \ 1 \ 0]^T$
T-FFT	3	3	1	$t_n = t/T - 1/2$	$t_n^2 - 1/12$	$[1 \ 0 \ 0]^T$

algorithm computes the weight vectors as  $\mathbf{a}_{k+1}^m = \mathbf{a}_k^m + \mathbf{g}_k^m e_k^{m*}$  where

$$\mathbf{g}_k^m = \frac{\frac{\mathbf{P}_k^m \mathbf{y}_k^m}{x_{k-1}^m}}{\lambda + \mathbf{y}_k^{mH} \mathbf{P}_k^m \mathbf{y}_k^m / |x_{k-1}^m|^2}. \quad (31)$$

Here,  $\lambda$  is the forgetting factor, and  $\mathbf{P}_k^m$  is the inverse of the correlation matrix of  $\mathbf{y}_k^m$  which is initialized as  $\mathbf{P}_0^m = \delta^{-1} \mathbf{I}$  ( $\delta$  is a small constant), and computed recursively across carriers as

$$\mathbf{P}_{k+1}^m = \lambda^{-1} \mathbf{P}_k^m - \mathbf{g}_k^m \left( \frac{\mathbf{y}_k^m}{x_{k-1}^m} \right)^H \lambda^{-1} \mathbf{P}_k^m. \quad (32)$$

Note that this algorithm invokes the assumption of independence between adjacent weight vectors, to obtain a linear relationship between the vector  $\mathbf{a}_k^m$  and the scaled input  $\mathbf{y}_k^m / x_{k-1}^m$ . Application of the RLS algorithm improves the performance in cases where correlation between combiner inputs limits the convergence speed of the stochastic gradient algorithm due to separation of eigenvalues, e.g., when using S-FFT demodulation.

### B. Compensation of Large Doppler Shifts: Carrier Sliding

The proposed Doppler compensation techniques are capable of reducing the effects of Doppler as long as the shift is not excessively large (large enough to slide the desired carrier out of reach of its combiner). Namely, F-FFT demodulation with  $I = 3$  can effectively compensate for any Doppler shift up to  $\Delta f/2$ , but its performance degrades if the Doppler shift exceeds this value. The other three proposed techniques have similar limits. Analysis of experimental data shows that the residual Doppler (after resampling) can be as much as 5 Hz, which is greater than the carrier spacing if  $2^{10}$  carriers are used ( $\Delta f = 4.75$  Hz). Such a Doppler shift would significantly degrade the performance of the proposed methods unless the combiner size is increased (see Fig. 10).

One approach to widen the range of Doppler shifts that can be compensated is to increase the size of the combiner. For example, choosing  $I = 2$  and  $L = 5$  for F-FFT demodulation would make it capable of compensating for Doppler shifts up to  $\Delta f$  as the inputs to combiner cover the frequency range  $[f_k - \Delta f, f_k + \Delta f]$ . However, such an approach comes at a penalty on receiver complexity and speed of convergence.

An alternative method is to monitor the Doppler shift and slide the carriers by one (or a fraction of a carrier for F-FFT) up or down if the Doppler shift is greater than a certain threshold. Doppler shift can be estimated through the set of combiner weights for each method. For P-FFT and S-FFT demodulation, sliding the carriers is beneficial if the Doppler shift is

greater than  $\Delta f/2$ . Doppler shift for these two methods can be estimated by comparing the phase of the first and the last combiner weight. If the difference in their phase is greater than  $(I - 1/I)\pi$ , the Doppler shift is deemed greater than  $\Delta f/2$  and carrier sliding is initiated.<sup>9</sup> Doppler shift can be similarly estimated for T-FFT by comparing the phase of the corresponding polynomial at  $t = 0$  and  $t = T$ , and the carriers should slide if the difference is greater than  $\pi$ . For F-FFT, there is no need for explicit Doppler estimation and sliding would be required simply if the middle combiner weight ceases to be the strongest.

Sliding the carriers effectively transforms the channel coefficient  $H_k^m(t)$  to  $H_k^m(t)e^{\pm j2\pi\Delta f t}$  (or  $H_k^m(t)e^{\pm j\pi\Delta f t}$  for half the carrier slides) and, therefore, the optimal combiner weights change. For P-FFT and S-FFT demodulation, we follow this change by multiplying the  $i$ th combiner weight by  $e^{\mp j2\pi((i+1/2)/I)}$  and for T-FFT demodulation, we fit a new polynomial to the original one shifted up or down by  $\Delta f$ . To update the combiner weights for F-FFT demodulation, we simply slide the combiner weights up or down (depending on the sign of the Doppler shift), where one of the combiner weights is discarded and the new weight is initiated with zero. Carrier sliding provides the flexibility of compensating for large Doppler shifts with minimum penalty on complexity, while maintaining the same convergence speed. This approach plays hand in hand with reusing combiner weights for initialization of new OFDM blocks to provide a robust detection method which can operate reliably, even when the residual Doppler shift (after initial resampling) exceeds the carrier spacing. Specifically, the proposed algorithms do so with small additional complexity (two or three FFTs).

### C. Initialization and Detection Order

For each method, the algorithm is initialized by a set of coefficients  $\mathbf{a}_0^m$  corresponding to conventional, single-FFT demodulation. Pilot symbols (10–20 times the combiner length suffice) are used initially after which the algorithm is switched into the decision-directed mode.

At the end of the first OFDM block, the vectors corresponding to the highest carrier  $\mathbf{a}_{K-1}^m$ ,  $m = 1, \dots, M$ , are saved and used to initialize the next block in which the recursion is carried out backwards, i.e., beginning from the highest carrier and moving on to the lowest. The process then repeats periodically as the new blocks come in. This order of detection, which is illustrated in Fig. 7, avoids insertion of pilots in every OFDM

<sup>9</sup>A more accurate approach is to linearly interpolate between the phases of each combiner's weights, and use the so-obtained slope to infer the Doppler shift. However, this approach did not show a significant effect on the overall performance.



TABLE II  
NUMBER OF MULTIPLICATIONS REQUIRED FOR EACH DETECTION METHOD

Method	Multiplications required for FFT(s)	Multiplications required for detection	Total number of multiplications compared to conv. diff. detection ( $K = 1024$ )	FEC decod. repetitions
Conventional diff	$2MK\log_2(K)$	$(16M + 8)K$	1.00 ( $I = 1, L = 1$ )	1
Equalized diff	$2MK\log_2(K)$	$(14L+24)MK$	2.21 ( $I = 1, L = 3$ )	1
P-FFT differential	$2IMK\log_2(K)$	$(14L+24)MK$	3.79 ( $I = 2, L = 6$ )	1
S-FFT differential	$2IMK(\log_2(K) + 2)$	$(14L+24)MK$	3.95 ( $I = 2, L = 6$ )	1
F-FFT differential	$2IMK\log_2(K)$	$(14L+24)MK$	2.79 ( $I = 2, L = 3$ )	1
T-FFT differential	$2IMK(\log_2(K) + 2)$	$(14L+24)MK$	3.32 ( $I = 3, L = 3$ )	1
Conv. coherent ([5])*	$6IMK\log_2(K)$	$48MK$	2.84 ( $I = 1, L = 1$ )	3
Eq. coherent ([2])*	$6IMK\log_2(K)$	$(48 + 4L^2 + 12L)MK$	4.74 ( $I = 1, L = 3$ )	4
resampling	-	$124MK$	3.26	-

\* Does not include sparsing of the estimated channel impulse response.

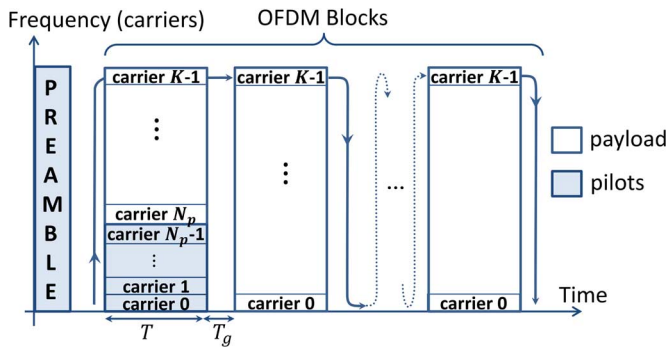


Fig. 7. Order of detection through one frame of OFDM blocks. Differential detection is carried out in increasing order across carriers for the first block and in decreasing order in the next. This process is repeated for the rest of the OFDM blocks. Such detection order eliminates the need for pilots in every OFDM block.

block, resulting in low total overhead (e.g., 0.3%–0.6% overhead for  $L = 3$  in MACE'10). Table I summarizes typical parameters used with the experimental data for each of the proposed methods.

#### D. Complexity Analysis

The complexity of the receiver for each method depends on the parameters  $I$  and  $L$ , the number of carriers  $K$ , and the number of receiver elements  $M$ . Table II summarizes the number of multiplications required for implementing each method. This table does not include the complexity of decoding for forward error correction (FEC) code, and the channel sparsing in coherent detection.

Table II shows that the typical complexity of implementing either of the proposed methods is no more than four times the complexity of conventional differential detection. We have also implemented P-FFT demodulation for differentially coherent receiver in C for use on DSP processors, and the processing time required to run P-FFT receiver with  $I = L = 2$  was measured to be roughly 2.5 times as much as that required for the conventional differentially coherent receiver, which agrees with the complexity calculations in Table II. Note also that the

proposed techniques do not require repetition of FEC decoding while coherent detection methods (as in [5] and [2]) repeat FEC decoding after each refinement of the channel estimate to enhance reliability.

#### V. SIMULATION RESULTS

In this section, we assess the average performance of the proposed differential detection methods through simulation and compare it to the conventional coherent and differentially coherent detection methods. We use full-VirTEX [18] to simulate the time-varying UWA channel. Full-VirTEX produces multiple channel realizations, spaced by  $\Delta T$  in time, for the duration of the transmitted signal. Each realization of the channel is made by the BELLHOP ray-tracing program [19]. The output of each BELLHOP run is the channel impulse response (and the angle of arrival for each path) over a 2-D grid in space which covers the region of the receiver motion. For each run, the environment and/or the receiver position changes slightly from the previous run, according to predefined parameters (transmitter/receiver trajectory and the wave motion). The channel responses from different instants are assembled together to form a 3-D mesh of channel responses, with two dimensions in space and one dimension in time. At each instant, full-VirTEX finds the smallest cube which contains the receiver position. The size of the cube is defined by the resolution of the 3-D mesh. Full-VirTEX then linearly interpolates among the eight corners of a cube where the channel response and angles of arrival are known, to estimate the channel response at the exact location of the receiver for that instant. Linear interpolation is based on the assumption of plane wave propagation for each path according to the path's angle of arrival.

We choose simulation geometries similar to those of MACE'10. Specifically, we use the recorded sound-speed profile (see Fig. 8), transmitter/receiver depth, and receiver array structure shown in Fig. 12. We choose the wave height to be 2 m peak-to-peak and the receiver to be approximately 1.5 km away from the transmitter. We produce five geometries which differ slightly in the shape of the seabed and surface

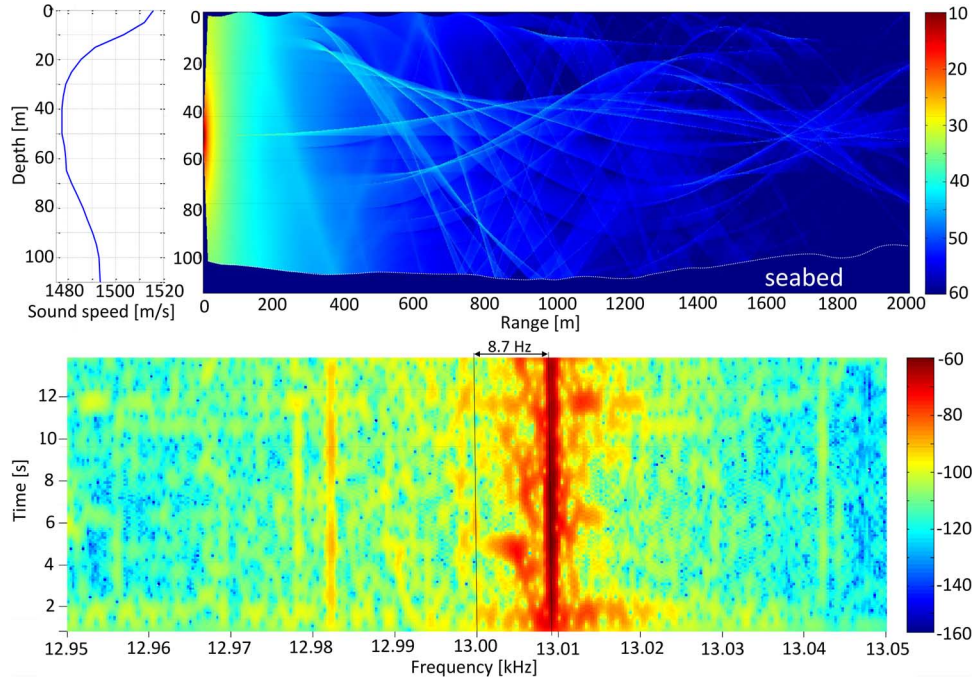


Fig. 8. Sound-speed profile measured during MACE'10 (top left) is used for simulations. Ray trace for one of the geometries used in our full-VirTEX simulation is shown on the right. The acoustic field intensity is shown for a tone of 13 kHz; speed of sound is 1400 m/s in the seabed (soft seabed), density of the seabed is  $1800 \text{ kg/m}^3$ , and the amplitude and length of the surface waves are 2 and 150 m, respectively. This plot also provides an insight into the propagation paths during MACE'10. Shown in the bottom plot is the spectrum of the signal received in response to the transmitted 13-kHz tone. The receiver is moving horizontally at the speed of 1 m/s toward the transmitter, which causes a Doppler shift of 8.7 Hz. The Doppler shifts caused by surface waves are also visible in the spectrum.

motion, analyze the performance of each method for each of the geometries, and report the average MSE performance results.

Fig. 8 shows the acoustic field intensity at 13 kHz for one of the channel geometries used for simulation. The bottom plot shows the spectrum of the received signal while a 13-kHz tone is transmitted. This spectrum clearly shows the Doppler distortion caused by motion of the transmitter/receiver and the surface. All of the simulations in this section are based on OFDM blocks with  $2^9$  carriers, transmitted over the acoustic frequency band 10.5–15.5 kHz. Motion is considered to occur at a constant speed during each frame. A frame starts and ends with a preamble and contains 16 OFDM blocks.

Fig. 9 shows the performance of P-FFT demodulation and compares it with that of conventional differentially coherent detection. Conventional detection method is very sensitive to motion-induced Doppler and will fail if the receiver moves faster than 0.1 m/s in this case. P-FFT demodulation, in contrast, adds robustness against Doppler shifts. Moreover, robustness improves with increasing the number of partial segments  $I$  and by applying equalization. If we choose  $I = 2$  and  $L = 6$ , the MSE stays below  $-5 \text{ dB}$ , i.e., sufficiently low to ensure satisfactory performance of subsequent data detection, for motion at speeds up to 0.75 m/s, at which the Doppler shift exceeds half the carrier spacing. Since carrier sliding helps in dealing with Doppler shifts greater than half the carrier spacing, we choose  $I = 2$  and  $L = 6$  to limit the receiver complexity (only two FFTs). Experimental results also support this choice of the combiner structure.

The average MSE performance for S-FFT and T-FFT demodulation follows a trend similar to P-FFT, showing improved performance as  $I$  and  $L$  increase. We choose  $I = 2$  and  $L = 6$  for

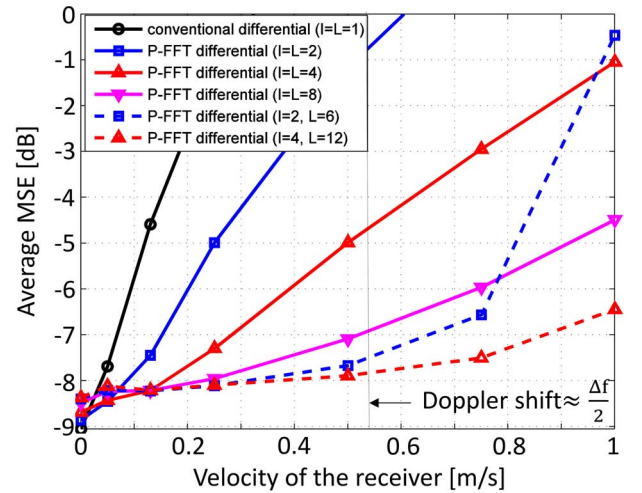


Fig. 9. MSE performance of conventional differential detection and differential detection with P-FFT demodulation for various combiner lengths versus speed of receiver motion. Five geometries are implemented for BELLHOP and full-VirTEX is used to simulate the receiver motion for each of the geometries. The MSE values represent an average over a total of  $4.1 \times 10^4$  QPSK data symbols. OFDM blocks in this simulation consist of  $2^9$  carriers, and four receiver elements spaced by 36 cm are utilized. The average SNR at the input to each of the receiver elements is 10 dB.

S-FFT and  $L = I = 3$  for T-FFT (i.e., quadratic approximation) as a tradeoff between performance and complexity.

Fig. 10 compares the various proposed methods in selected configurations to conventional coherent and differentially coherent detection methods. In addition, we have included as a benchmark differentially coherent detection with linear equalization (LE) implemented using a combiner identical to the one used for the other methods. Without any motion in the channel,

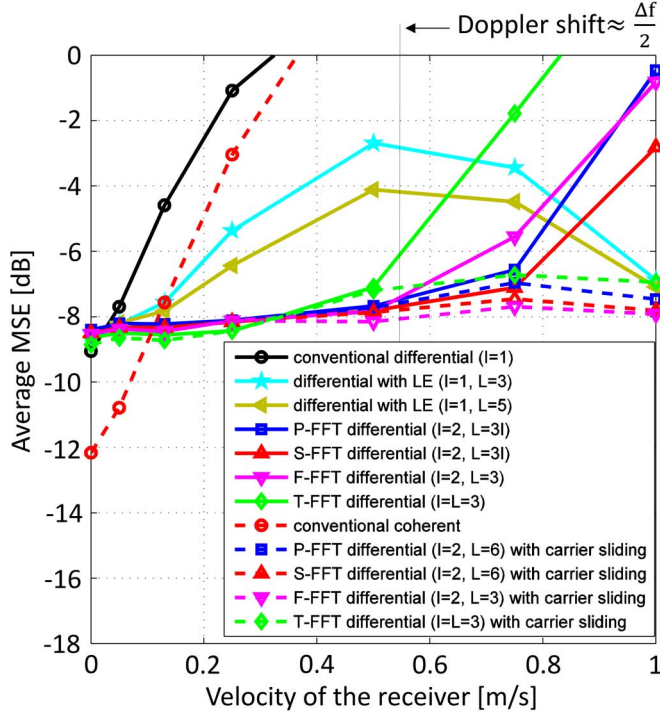


Fig. 10. Comparison of various receiver algorithms: conventional coherent and differentially coherent (with and without equalization), and differentially coherent detection with multiple-FFT demodulation with and without carrier sliding. System parameters are the same as those of Fig. 9.

coherent detection provides the best performance and pre-FFT compensation is not necessary. However, as receiver motion is introduced, performance degrades. The performance of conventional differential detection similarly degrades with motion. Application of three- or five-tap equalizer can help improve the performance, but as the speed of motion increases and Doppler shift approaches half the carrier spacing, the performance degrades significantly. At such speeds, all of the four proposed methods outperform coherent and differentially coherent detections with a significant margin. Among the proposed methods in this figure, F-FFT is implemented with the least complexity ( $I = 2$  and  $L = 3$ ) and since it is virtually insensitive to any Doppler shift smaller than half the carrier spacing, it is not necessary to increase the number of FFT demodulators or the combiner length.

As the Doppler shift increases beyond half the carrier spacing, it eventually reaches a full carrier spacing, and the LE with either three or five taps captures the energy of the carrier-shifted data symbol, thus bringing the MSE down. The other methods, if not aided by carrier sliding, lose the desired data symbol from view. However, aided by carrier sliding, they outperform LE.

Finally, Fig. 11 shows the average MSE as a function of the input SNR for a fixed receiver velocity. This result asserts that increasing the SNR will not compensate for the effect of ICI. Conventional coherent and differentially coherent receivers will not have successful detection at any SNR if the motion is faster than 0.2 m/s. Conventional equalization can improve the performance to some extent but the penalty in the performance (due to motion) is still significant. In contrast, the performance of the proposed multiple-FFT methods improves almost linearly with SNR. Specifically, at the input SNR above 15 dB, no detection

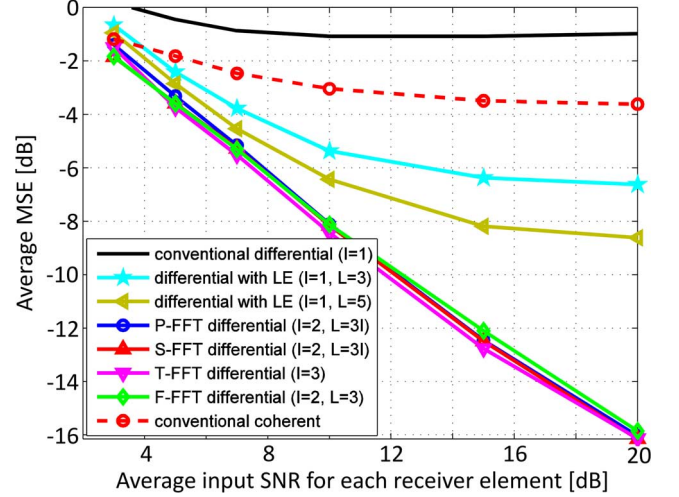


Fig. 11. Average MSE performance of conventional detection methods and the multiple-FFT methods versus the input SNR. The receiver moves away from the transmitter at 0.25 m/s, resulting in the lowest carrier's Doppler shift of about 4.5 Hz which is approximately  $\Delta f/4$ . System parameters are the same as in Fig. 9.

errors were observed for any of the five geometries used for simulation.

## VI. EXPERIMENTAL RESULTS

In this section, we provide the results from MACE'10 which was conducted during summer 2010, about 60 mi south of Rhode Island, USA, using the acoustic frequency range between 10.5 and 15.5 kHz. Fig. 12 shows the approximate channel geometry, the structure of the receiver array, and the path along which the transmitter moved during the experiment. Signal parameters are summarized in Table III. The results provided in this section are obtained from all 52 transmissions which took place every 4 min during the 3.5-h experiment (a total of  $4.26 \times 10^5$  QPSK symbols). The input SNR for each receiver element varies between 7 and 20 dB, depending on the distance between the transmitter and the receiver, and the state of the channel (fading). We report on the average MSE performance rather than a set of isolated cases so as to offer insight into a broad range of situations. The evolution of the MSE in time, as well as the corresponding estimated cumulative probability density function (CDF) will also be summarized to illustrate the dispersion around the average.

### A. Initial Synchronization and Resampling

Initial synchronization is typically based on the preambles transmitted at the beginning of each frame [1]. Unlike in [1], where the peak of correlation between transmitted and received preambles is used to determine the start and end of a frame, we employ a method based on weighted averaging of sparsed correlation metrics. Specifically, let us denote by  $R_1(\tau)$  the sparsed and normalized correlation between the transmitted preamble (a high-resolution broadband signal) and its received copy. Sparsing is applied according to the low complexity thresholding method described in [20] where the sparsing threshold is optimized to be just above the noise level. Normalization ensures that  $\int_{T_{\text{sync}}} |R_1(\tau)| d\tau = 1$ , where  $T_{\text{sync}}$  is the interval over which the correlation is observed.



TABLE III  
OFDM SIGNAL PARAMETERS USED FOR MACE'10. BANDWIDTH EFFICIENCY IS CALCULATED FOR THE GUARD INTERVAL  $T_g = 16$  ms. THE TOTAL BANDWIDTH IS  $B = 5$  kHz, AND THE LOWEST CARRIER FREQUENCY IS  $f_0 = 10.5$  kHz

No. of carriers, $K$	64	128	256	512	1024	2048
No. of blocks per frame	128	64	32	16	8	4
carrier spacing $\Delta f$ [Hz]	76	38	19	9.5	4.8	2.4
block duration [ms]	13.1	26.2	52.4	105	210	419
transmission rate [kbps]	4.4	6	7.5	8.5	9	9.4
bandwidth eff. [bps/Hz]	0.9	1.24	1.53	1.74	1.86	1.93

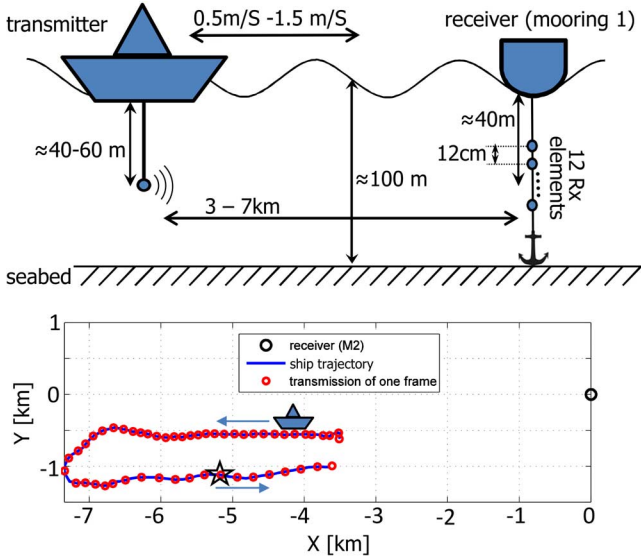


Fig. 12. Top: Nominal geometry of MACE'10. Bottom: trajectory of the transmitter. Receiver location is indicated by the large circle on the right at location (0,0). The transmitter first moves away from the receiver, then toward the receiver. This process takes approximately 3.5 h, during which there are 52 transmissions every 4 min (small circles). Every transmission consists of six frames of OFDM blocks and each of the frames contains in total  $2^{13}$  differentially encoded QPSK symbols. The six frames belonging to one transmission differ in the number of carriers that they use, which ranges from  $2^6$  to  $2^{11}$ . The number of blocks per frame also varies (see Table III). The star shows the location from which the frame that will be discussed in Fig. 19 was transmitted.

The starting time of the preamble is now determined as the weighted average

$$\tau_1 = \int_{T_{\text{sync}}} |R_1(\tau)| \tau d\tau. \quad (33)$$

To estimate the Doppler compression/dilation, we first measure  $R_2(\tau)$ , the sparsed and normalized correlation between the transmitted postamble (preamble of the next frame) and its received copy. To measure  $R_2(\tau)$ , we observe the correlation over the interval  $T_{\text{sync}}$  shifted forward by the nominal length of the frame,  $T_{\text{tx}}$ . We now estimate the length of the received frame as  $T_{\text{rx}} = T_{\text{tx}} + \Delta\tau_{1,2}$ , where

$$\Delta\tau_{1,2} = \arg \max_{\Delta\tau} R_{1,2}(\Delta\tau)$$

and

$$R_{1,2}(\Delta\tau) = \int_{T_{\text{sync}}} |R_1(\tau) R_2(\tau + T_{\text{tx}} - \Delta\tau)| d\tau. \quad (34)$$

The estimated frame duration is used to resample the signal by the factor  $T_{\text{rx}}/T_{\text{tx}}$ . This signal is fed to the FFT demodulators.

Fig. 13 compares synchronization based on the correlation peak [1] and the proposed method for one specific frame of MACE'10. The earlier multipath arrival appears as stronger at the beginning of this frame, but the later arrival takes over by the end of the frame, causing the peak method to fail (Doppler factor estimation error of more than 200%). The weighted average method, however, estimates the Doppler factor accurately for this specific frame as well as all other frames received during MACE'10. Synchronization results are also consistent across all the receiving elements. In the example of Fig. 13, the received frame is 0.75 ms longer than the transmitted frame (the duration of the transmitted frame is  $T_{\text{tx}} = 1897$  ms), which implies that the transmitter has been moving away from the receiver at the speed of about 0.6 m/s, resulting in a Doppler scaling factor of  $3.9 \times 10^{-4}$ .

Resampling the signal at a constant rate removes the Doppler distortion effectively if the only source of Doppler distortion is motion at a constant speed. However, in practical scenarios, the Doppler factor may be time varying due to the random motion of the transmitters, receivers, and scattering points. Therefore, initial resampling often targets coarse compensation of the motion-induced Doppler scaling, and a raw Doppler factor on the order of  $10^{-3}$  (relative transmitter/receiver velocity on the order of 1.5 m/s) will leave a residual Doppler factor that may be on the order of  $10^{-4}$ . For example, the maximum residual Doppler factor for the frame shown in Fig. 13 is approximately  $5 \times 10^{-5}$ , which is eight times smaller than the original Doppler factor. This remaining Doppler distortion is treated by fine signal processing, i.e., by the P-FFT, S-FFT, F-FFT, or T-FFT demodulation.

## B. Results

To establish a benchmark, Fig. 14 compares the average MSE performance of conventional differential detection and conventional coherent detection proposed in [5]. This figure shows the average MSE as a function of the number of carriers (log scale) for a varying number of receiving elements, which are chosen among the 12 available elements as equally spaced. Increasing the number of receiving elements from one to two, or from two to four, results in significant performance enhancement. However, the performance improvement obtained by increasing the number of receiving elements over a given aperture will eventually saturate as the signals of neighboring elements become correlated when element spacing is reduced. Therefore, increasing

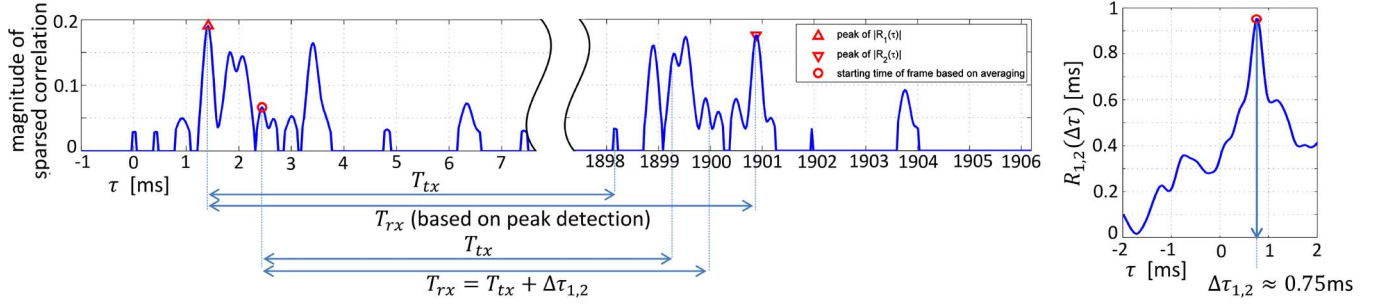


Fig. 13. Synchronization based on correlation peak detection estimates the start/end of a frame as the points where the preamble/postamble correlation peaks, and infers the frame duration  $T_{rx}$  from the time difference. Synchronization based on weighted averaging estimates the start of a frame according to (33). The frame duration is inferred from the peak of the function  $R_{1,2}(\Delta\tau)$  shown on the right, which indicates the amount of time compression/dilation  $\Delta\tau_{1,2}$  specified by (34). In this example, the strongest arrival is not the same during the preamble/postamble, causing failure of the peak detection method.

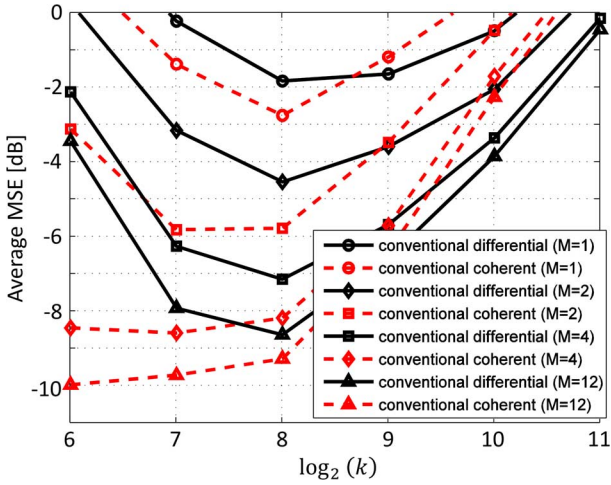


Fig. 14. Average MSE performance of conventional ( $I = L = 1$ ) differential detection and conventional coherent detection [5] versus the number of carriers  $K$  for a varying number of receiving elements. MSE values represent the average over all carriers and 52 frames transmitted over 3.5 h.

from four to 12 elements (and thus reducing the element spacing to 12 cm) provides significantly less gain for both methods.

Based on Fig. 14, we choose to utilize four elements out of the 12 available to limit the receiver complexity. With a small number of carriers (i.e., 64 or 128), coherent detection outperforms differential detection, because short OFDM blocks allow for effective channel tracking, while differential detection fails due to wide carrier separation which does not satisfy the basic frequency coherence requirement. This is of no concern, however, because the small number of carriers corresponds to lower bandwidth efficiency. As the number of carriers grows, differential detection gains advantage over coherent detection, eventually outperforming it as coherent detection starts to suffer from channel estimation errors (due to insufficient coherence between adjacent OFDM blocks). However, beyond  $2^9$  carriers, both detection methods fail due to ICI. In this region, which offers more frequency coherence for differential detection, we expect the proposed methods to mitigate the ICI and recover the performance.

Fig. 15 demonstrates the performance of S-FFT demodulation with differentially coherent detection. When carrier spacing is large (e.g.,  $K = 2^6$ ), there is very little ICI and, therefore, S-FFT demodulation provides little to no gain. However, as the number of carriers is increased, ICI becomes more significant

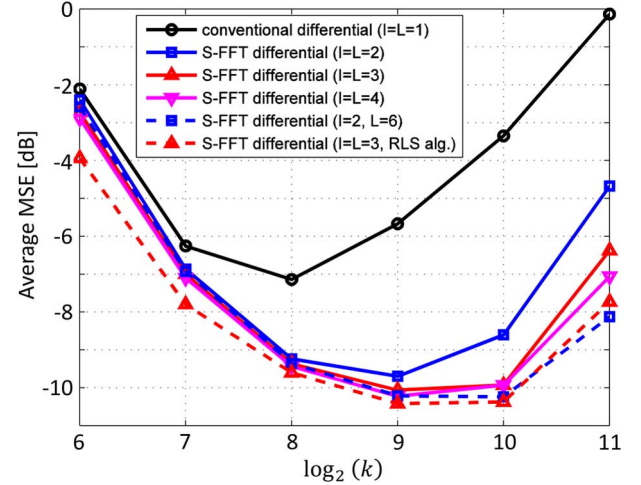


Fig. 15. Average MSE performance of S-FFT demodulation for a varying number of FFT demodulators ( $I$ ) and combiner size ( $L$ ), obtained using the MACE10 data. This figure also demonstrates the additional gain that may be achieved by employing RLS algorithm instead of the stochastic gradient algorithm.  $M = 4$  receiver elements were used. MSE values represent the average over all carriers and 52 frames transmitted during 3.5 h.

and eventually results in failure of conventional differential detection at  $2^{10}$  carriers. This is where S-FFT demodulation with two FFTs ( $I = 2$ ) provides more than 5-dB gain compared to conventional differential detection. Including a three-tap equalizer ( $I = 2, L = 6$ ) increases the gain to 7 dB. With  $I = L = 4$ , S-FFT demodulation can almost match this performance, but increasing  $I$  would require additional FFT demodulators, thus increasing the receiver complexity. Considering the additional complexity, we choose  $I = 2$  and  $L = 6$  as a good tradeoff between complexity and performance for this method.

P-FFT demodulation follows a similar trend and delivers good performance with  $I = 2$  and  $L = 6$ . The advantage of S-FFT over P-FFT is the smooth transition between segments, which comes at the cost of a small correlation between adjacent segments (due to the overlap of decomposition functions; see Fig. 4). Smooth transition improves the accuracy of channel decomposition, but the correlation reduces the convergence speed of the adaptive algorithm. Therefore, when  $I$  is small and the accuracy of decomposition limits the performance, we expect S-FFT demodulation to outperform P-FFT demodulation, but when  $I$  is large and speed of convergence is the limit, we expect the opposite effect. In this situation, the RLS algorithm enhances the performance as it converges faster



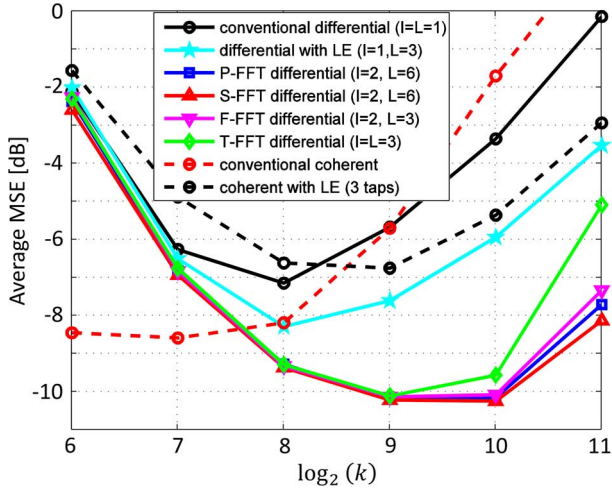


Fig. 16. Average MSE performance of differentially coherent detection with P-FFT, S-FFT, F-FFT, and T-FFT demodulation in comparison to conventional detection methods for the MACE'10 data.  $M = 4$  receiving elements were used. MSE values represent the average over all carriers and 52 frames transmitted over 3.5 h. All four multiple-FFT methods are shown to be competitive in reducing the effect of Doppler distortion. Differentially coherent detection with either of the compensation methods outperforms conventional methods (coherent and differentially coherent, with or without LE).

than the stochastic gradient algorithm, providing an additional 0.5–1.5-dB gain in the performance.

The performance of all four methods in selected configurations is summarized in Fig. 16. F-FFT is implemented using  $I = 2$  and  $L = 3$ , which was shown to be virtually insensitive to Doppler shifts smaller than half the carrier spacing (see Fig. 10). Larger Doppler shifts are compensated by sliding the carriers up or down (see Section IV-B), and, therefore, there is no need to increase  $L$ . T-FFT is implemented using quadratic decomposition ( $I = L = 3$ ) which improves the performance of differentially coherent detection by 7 dB. This selection agrees with the one made in [16] that quadratic decomposition suffices for expressing channel variations in time and frequency domain with reasonable accuracy. In addition to the comparison with conventional methods, we include the ICI equalization method [2] for coherent and differentially coherent detections. This method consists of two steps: primary conventional coherent detection (ICI-ignorant) and linear ICI equalization. Here, we employ the coherent detection method [5] as the primary detection method. In the second step, reestimation process takes advantage of an equalizer with three (or more) taps and uses the decisions of the primary detector as pilots. Each equalizer tap is estimated independently in a carrier-by-carrier fashion, through stochastic gradient algorithm operating jointly with a second-order phase-locked loop for tracking the phase across carriers. The equalizer is initialized independently for each OFDM block and learns the equalizer taps carrier by carrier. In what follows, we call this algorithm coherent detection with LE.

Fig. 16 shows that as long as the length of the OFDM block is sufficiently short, conventional coherent detection outperforms all other methods. All differential detection techniques and the coherent detection with LE rely on coherence between carriers which is not justified with wide carrier spacing. In fact, coherent detection with LE suffers more severely from wide carrier spacing compared to differential detection because it

relearns the channel and equalizer taps through a stochastic gradient algorithm, making it dependent on coherence between carriers. As the number of carriers is increased and OFDM blocks become longer, the conventional coherent detection method starts to suffer from insufficient coherence between adjacent blocks, while all differential detection methods and coherent detection with LE enjoy the increased coherence between carriers. Eventually, as the number of carriers grows to  $K = 2^{11}$ , our proposed methods, coherent and differentially coherent detection with LE, and conventional differential detection outperform conventional coherent detection at  $2^8$ ,  $2^9$ , and  $2^{10}$  carriers, respectively. Multiple-FFT demodulation methods clearly offer the best performance, with a 3–5-dB gain over detection methods with LE.

Setting the MSE bar at some value required for subsequent decoding to yield an acceptable bit error rate (BER), say  $-5$  dB, Fig. 16 implies the range of carriers that can be supported by each of the methods. While conventional coherent detection favors a small number of carriers (up to 512), the proposed pre-FFT compensation techniques open this range up (to 2048), thus increasing the bandwidth efficiency. We alluded to this fact in the introductory discussion and illustrated it conceptually in Fig. 1. The results of Fig. 16 provide a matching quantitative measure.

Although linear equalization has some success in reducing the ICI for both coherent and differentially coherent detection with  $2^9$  and  $2^{10}$  carriers, it eventually fails with  $2^{11}$  carriers. Analysis of the experimental data reveals that the prime reason for failure of coherent detection with LE is the limitation of the primary (ICI-ignorant) detection in the presence of ICI. This algorithm disposes of the equalizer weights after each OFDM block and relies on conventional detection as its only source of pilots during the next OFDM block. A Doppler shift on the order of  $\Delta f/2$  will result in failure of primary detection, depriving carrier-by-carrier equalization of reliable pilots and the chance to converge.

The proposed multiple-FFT algorithms, in contrast, achieve excellent performance with the MACE'10 data with  $2^8$ ,  $2^9$ , and  $2^{10}$  carriers. These algorithms simply store the combiner weights and reuse them to initialize the detection of the next OFDM block. Such a choice is justified by the fact that a severe change in Doppler shift between adjacent blocks occurs only if the motion of the transmitter or the receiver has rapid acceleration. For example, with  $2^9$  carriers in a bandwidth of 5 kHz (as in MACE'10), the duration of each OFDM block is about 0.1 s. Assuming an acceleration of  $1 \text{ m/s}^2$ , the Doppler shift will change by as much as 0.87 Hz during one OFDM block, which is a small fraction of the carrier spacing ( $\Delta f \approx 10 \text{ Hz}$ ).

As the number of carriers grows beyond  $2^{10}$ , the performance of all algorithms degrades due to severe ICI. However, the proposed algorithms deliver good average performance even with  $2^{11}$  carriers ( $\Delta f \approx 2.5 \text{ Hz}$ ), although residual Doppler shifts can be many times greater than the carrier spacing. Specifically, F-FFT demodulation delivers such performance at minimal additional complexity (two FFTs and a three-tap combiner). This performance owes to a dedicated mechanism for sliding the carriers in the presence of large Doppler shifts, which we will describe in Section VI-C. Before we do so, let us complete the

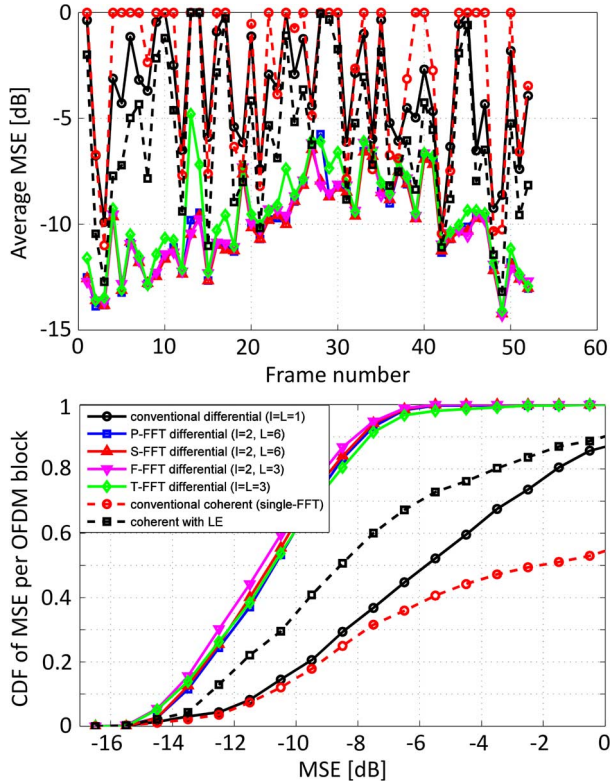


Fig. 17. Time evolution (top) and the estimated CDF of MSE for multiple demodulation techniques (bottom). The CDFs reflect all 52 transmissions with  $2^{10}$  carriers during MACE'10. Conventional coherent detection has success (MSE  $< -5$  dB) with fewer than half of the OFDM blocks. Linear equalization reduces the chances of losing the track, but fails for OFDM blocks which suffer from severe ICI. Conventional differentially coherent detection slightly outperforms coherent detection by delivering an MSE below  $-5$  dB for more than half of the OFDM blocks. Applying either of the multiple-FFT demodulation techniques to differentially coherent detection boosts the MSE performance to the range between  $-15$  and  $-5$  dB in more than 99% of all cases (52 frames transmitted over 3.5 h).

MSE analysis by commenting on the issue of the instantaneous MSE, i.e., the variation of the MSE around the average value.

Fig. 17 illustrates the time evolution of the MSE and provides the corresponding CDF. The instantaneous MSE is defined as the MSE per block (average over all carriers). Time evolution is illustrated using additional averaging over the blocks of one frame so as to avoid crowding, while the CDF is that of the instantaneous MSE. The figure refers to the case with  $2^{10}$  carriers, and includes the 52 frames ( $4.26 \times 10^5$  data symbols) transmitted over 3.5 h. This result shows that all of the multiple-FFT demodulation methods perform consistently between  $-15$ - and  $-5$ -dB MSE. Specifically, F-FFT slightly outperforms the other methods, maintaining the MSE under  $-5$  dB for 99% of the OFDM blocks. Without multiple-FFT demodulation, coherent and differentially coherent detections deliver MSE below  $-5$  only for 43% and 60% of the OFDM blocks, respectively. Linear equalization improves the MSE of coherent detection significantly for the cases where primary detection succeeds in tracking the channel. It reduces the chance of losing track of the channel for the following OFDM block, but for many of the OFDM blocks primary detection eventually fails due to ICI. The MSE is thus kept below  $-5$  dB in 70% of the cases.

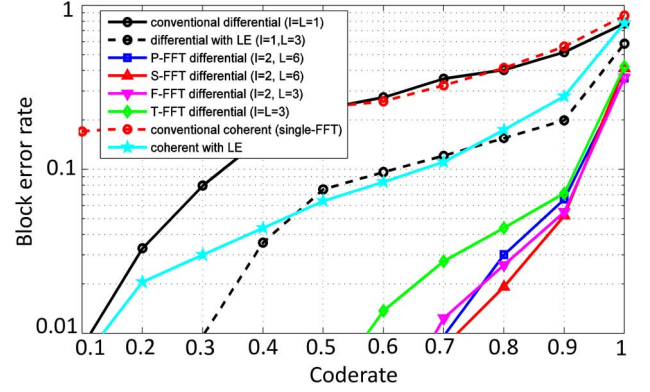


Fig. 18. Estimated BLER versus the rate of the LDPC code for different detection techniques. The results reflect all 52 transmissions with  $2^{10}$  carriers during MACE'10. The proposed methods can achieve very good performance with BLER  $< 2.5\%$  using code rates as high as 0.8. Conventional detection methods can only deliver such reliability at much lower code rates. Specifically, conventional coherent detection cannot deliver BLERs below 15% with any code rate due to vulnerability of channel tracking to ICI.

Fig. 18 shows the BLERs achievable using regular low-density parity-check (LDPC) codes. The LDPC codes are designed so that each codeword fills one OFDM block, and decoding is based on the maximum *a posteriori* probability (MAP) rule using belief propagation [21]. This figure demonstrates the tradeoff between the throughput and reliability for each detection technique. As an example, if the BLER is required to be below 2%, differentially coherent detection with either S-FFT or F-FFT demodulation may be used with a code rate of 0.8, delivering 7.2 kb/s over a bandwidth of 5 kHz. Differentially coherent detection with LE can match the reliability with a code rate of 0.2, delivering 1.8 kb/s, or it can deliver 7.2 kb/s with reduced reliability (BLER = 16%).

### C. Carrier Sliding

In Fig. 19, we take a closer look at the way in which the proposed methods operate. Shown in this figure are the phases or amplitudes of the weight coefficients  $a_k^m$  for the first receiver element as they evolve over time (OFDM blocks) and carriers. The first 40–80 carriers of the first block are devoted to pilot symbols; the rest of the operation occurs in the decision-directed mode. At the beginning of the frame, all methods show presence of a large positive Doppler shift. If the dominant source of time variation is the small residual Doppler shift, then one expects the P-FFT and S-FFT combiner weights to match the resulting phase distortion. Fig. 19 indeed demonstrates such behavior for these two methods. For F-FFT demodulation, as the Doppler shift occurs, coefficients other than the middle one gain weight, and as the Doppler exceeds quarter of the carrier spacing, the middle coefficient is no longer the strongest. Again, Fig. 19 shows such a behavior for F-FFT demodulation. As far as T-FFT is concerned, suffice it to mention that the presence of Doppler results in all coefficients gaining weight, as compared to having a single nonzero coefficient in the absence of Doppler.

In Fig. 19, F-FFT demodulation applies a slide of  $\Delta f/2$  at the 38th carrier of the first OFDM block, which is within the range of pilot carriers. Doppler increases through the rest of the first OFDM block, exceeding  $\Delta f/2$ , and S-FFT demodulation

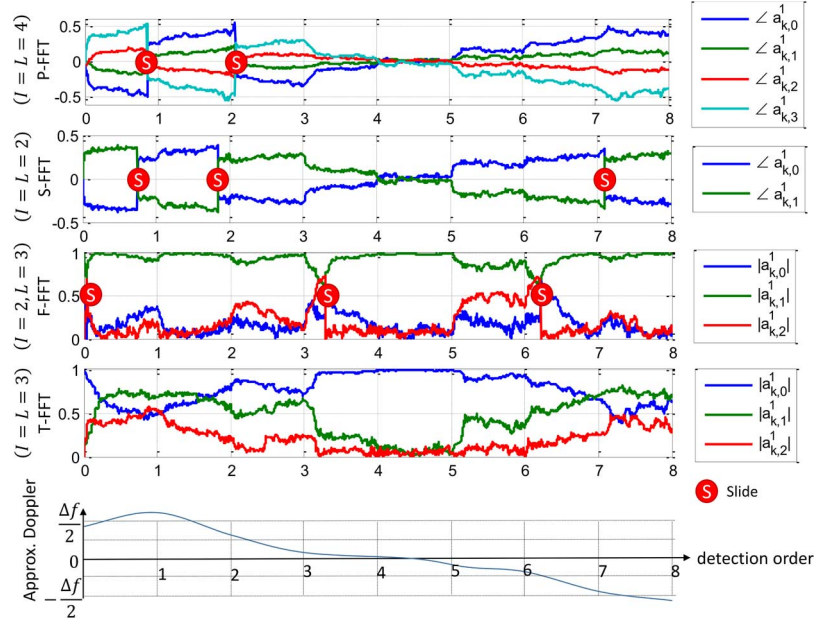


Fig. 19. Evolution of combiner weights corresponding to one receiving element ( $m = 1$ ) as detection proceeds over carriers and OFDM blocks (as shown in Fig. 7) during one frame with  $2^9$  carriers for the first receiver element. The plots show the phase of  $\mathbf{a}_k^1$  for P-FFT and S-FFT demodulation, the magnitude of  $\mathbf{a}_k^1$  for F-FFT and T-FFT demodulation, and estimated Doppler shift. The numbers of carriers required for convergence of P-FFT, S-FFT, F-FFT, and T-FFT demodulation methods are 55, 15, 45, and 40, respectively. S-FFT converges faster than the other methods as it has the shortest combiner. At the beginning of the first OFDM block, F-FFT detects a positive Doppler shift greater than  $\Delta f/4$  and slides the carriers up by half the carrier spacing. Doppler shift increases to more than  $\Delta f/2$  during the first OFDM block and S-FFT is the first to detect the requirement for sliding the carriers. During this OFDM block, T-FFT also shows presence of a Doppler shift, but no carrier sliding occurs. At this time, F-FFT shows very little Doppler as half the carrier slide applied at the beginning of the block matches the approximate Doppler shift during the first three OFDM blocks. By the end of the second OFDM block, Doppler shift decreases to less than  $\Delta f/2$  and S-FFT (followed by P-FFT) slides the carriers down (back to the nominal arrangement). The rest of the frame follows in a similar manner as the Doppler shift decreases, changes sign during the fifth OFDM block (where all four methods show insignificant Doppler shift), then grows in the opposite direction until the end of the frame, resulting in downward carrier sliding for F-FFT and S-FFT demodulation methods.

applies a slide of  $\Delta f$  on the 770th carrier, followed by P-FFT demodulation which slides the carriers on the 881st carrier. Note that the slide occurs sooner for F-FFT demodulation (at  $\Delta f/4$ , compared to  $\Delta f/2$  for the other three methods). Doppler shift decreases during the second and third OFDM blocks and results in both P-FFT and S-FFT demodulation sliding the carriers back to nominal. The Doppler shift continues to decline through the fourth and fifth OFDM blocks, resulting in F-FFT demodulation also sliding the carriers back to nominal during the fourth OFDM block. The rest of the frame continues with an increasing negative Doppler shift which results in F-FFT and S-FFT making a slide again. The slower convergence of P-FFT demodulation (which is due to its longer combiner) prevents it from reaching the threshold for sliding carriers again before the end of the frame. Similarly, T-FFT does not initiate carrier sliding, but instead compensates for the Doppler on its own. It does so successfully so long as the number of carriers is below 1024, but suffers some performance degradation thereafter (see Fig. 16).

The frame shown in Fig. 19 suffers a maximum Doppler shift of more than  $\Delta f/2$  (equivalent to Doppler factor of  $2 \times 10^{-4}$ , or motion at 0.3 m/s) at the end of the first OFDM block which is one of the extreme cases of residual Doppler in MACE'10 (transmitter location indicated by the star in Fig. 12). The MSE performance for this specific frame remains excellent at  $-9.8$ ,  $-10$ ,  $-10.5$ , and  $-9$  dB for P-FFT, S-FFT, F-FFT, and T-FFT demodulation methods, respectively.

These results demonstrate the effectiveness of F-FFT demodulation in compensating for large Doppler shifts, confirming

simulation results of Fig. 10 where F-FFT is observed to be virtually insensitive to Doppler shifts smaller than half the carrier spacing. However, P-FFT, S-FFT, and T-FFT have the capability of compensating for the time variations of the amplitude of the channel coefficients as well. Therefore, selection of the best method to use depends on the actual channel. However, the difference in their performance is small, so this choice is not a critical one. What is important to note is that all methods achieve a substantial gain over their conventional counterparts.

## VII. CONCLUSION

We considered differentially coherent detection of acoustic OFDM signals and proposed four demodulation methods for channels with severe Doppler distortion where random, time-varying frequency shifts can be comparable with the carrier spacing. Instead of the conventional, single-FFT demodulation, these methods use multiple-FFT demodulators where the input to each FFT is a specific transformation of the received signal.

The type of transformation—windowing in time, frequency-shifting, projection onto series functions—defines the particular method as the partial (P), shaped (S), fractional (F), or Taylor series (T) FFT demodulation. Regardless of the choice of transformation, the demodulator outputs are combined in a manner that minimizes postdetection error. In particular, we have focused on differentially coherent detection, as it eliminates the need for explicit channel estimation, thus increasing the system robustness on rapidly varying channels. Differential encoding was performed in the frequency domain, and multiple receiving elements were used to perform differentially coherent MRC. For



MACE'10, we also proposed a new technique for initial synchronization, which is based on estimating the delay and time compression/dilation from a weighted sum of multipath arrivals.

The performance of the four proposed demodulation methods was compared to that of conventional detection (coherent and differentially coherent) using simulation and experimental data. The proposed methods were also compared to a coherent and differentially coherent detection methods which employ linear ICI equalization. Simulation results, as well as experimental results obtained using the MACE'10 data, have clearly shown the effectiveness of multiple-FFT demodulation in compensating for the motion-induced time variation of the channel. Specifically, excellent performance was achieved with real data using four receiving elements and up to 1024 carriers (average MSE observed over  $4.26 \times 10^5$  data symbols transmitted over 3.5 h was about  $-10$  dB, and BLERs of about 2.5% using LDPC FEC with a code rate of 0.8). Even with 2048 carriers, where the residual Doppler shift can be greater than twice the carrier spacing, P-FFT, S-FFT, and F-FFT demodulation techniques delivered very good average MSE performance of  $-8$  dB. Without either the receiver array (spatial diversity), the multiple-FFT demodulation, or accurate synchronization and resampling, successful reception was not possible.

In addition to providing improvement in performance over conventional detection, the proposed methods enable operation with a greater number of carriers, thus increasing the bandwidth utilization. Most notably, the proposed demodulation methods make differentially coherent detection feasible, which in turn eliminates the need for explicit channel estimation and requires only minimal complexity (a few FFTs and a simple stochastic gradient algorithm for differential detection). It thus offers an appealing solution for real-time implementation in high-rate, mobile underwater acoustic systems.

## APPENDIX

This Appendix provides the details of reduced-size MMSE ICI equalization for OFDM receivers with and without channel-matched filtering.

Considering a receiver with conventional single-FFT demodulator (no channel-matched filtering) and an equalizer with  $J \leq K$  taps covering carriers  $k - J^-$  through  $k + J^+$ , the data symbols are estimated as

$$\hat{d}_k = \mathbf{q}_{yk}^H \mathbf{y}_k \quad (35)$$

where the input vector  $\mathbf{y}_k = [y_{k-J^-} \cdots y_{k+J^+}]^T$  and the vector of equalizer coefficients  $\mathbf{q}_{yk} = [q_{k,-J^-} \cdots q_{k,J^+}]^T$  are of length  $J$ . The input vector  $\mathbf{y}_k$  is given by

$$\mathbf{y}_k = \sum_{l=0}^{K-1} \mathbf{r}_y(k, l) d_l + \mathbf{z}_k \quad (36)$$

where  $\mathbf{r}_y(k, l) = [R_y(k - J^-, l) \cdots R_y(k + J^+, l)]^T$  is a vector containing  $J$  elements of the  $l$ th column of  $\mathbf{R}_y$  and  $\mathbf{z}_k$  is circularly symmetric, zero-mean, complex Gaussian noise ( $J$

elements of the original noise vector  $\mathbf{z}$ ). The MMSE solution for the equalizer coefficients is

$$\mathbf{q}_{yk} = \left[ \sum_{l=0}^{K-1} \mathbf{r}_y(k, l) \mathbf{r}_y^H(k, l) + 2N_0 \mathbf{I} \right]^{-1} \mathbf{r}_y(k, k) \quad (37)$$

and the resulting MMSE is

$$E_y = 1 - \frac{1}{K} \sum_{k=0}^{K-1} \mathbf{r}_y^H(k, k) \mathbf{q}_{yk}. \quad (38)$$

Reduced-size MMSE equalizer for the receiver with channel-matched filtering is derived in a similar manner, yielding

$$\mathbf{q}_{vk} = \left[ \sum_{l=0}^{K-1} \mathbf{r}_v(k, l) \mathbf{r}_v^H(k, l) + 2N_0 \mathbf{R}_v(k) \right]^{-1} \mathbf{r}_v(k, k) \quad (39)$$

where

$$\mathbf{R}_v(k) = [\mathbf{r}_v(k, k - J^-) \cdots \mathbf{r}_v(k, k + J^+)] \quad (40)$$

and

$$\mathbf{r}_v(k, l) = [R_v(k - J^-, l) \cdots R_v(k + J^+, l)]^T. \quad (41)$$

The resulting MMSE is

$$E_v = 1 - \frac{1}{K} \sum_{k=0}^{K-1} \mathbf{r}_v^H(k, k) \mathbf{q}_{vk}. \quad (42)$$

Fig. 2 reflects numerical evaluation of equations (38) and (42).

## REFERENCES

- [1] B. Li, S. Zhou, M. Stojanovic, L. Freitag, and P. Willett, "Multicarrier communication over underwater acoustic channels with nonuniform Doppler shifts," *IEEE J. Ocean. Eng.*, vol. 33, no. 2, pp. 198–209, Apr. 2008.
- [2] K. Tu, D. Fertonani, T. Duman, M. Stojanovic, J. Proakis, and P. Hursky, "Mitigation of intercarrier interference for OFDM over time-varying underwater acoustic channels," *IEEE J. Ocean. Eng.*, vol. 36, no. 2, pp. 156–171, Apr. 2011.
- [3] J. Huang, S. Zhou, J. Huang, C. Berger, and P. Willett, "Progressive inter-carrier interference equalization for OFDM transmission over time-varying underwater acoustic channels," *IEEE J. Sel. Top. Signal Process.*, vol. 5, no. 8, pp. 1524–1536, Dec. 2011.
- [4] A. Radosevic, T. Duman, J. Proakis, and M. Stojanovic, "Selective decision directed channel estimation for UWA OFDM systems," in *Proc. IEEE Allerton Conf. Commun. Control Comput.*, Sep. 2011, pp. 647–653.
- [5] M. Stojanovic, "MIMO OFDM over underwater acoustic channels," in *Proc. 46th Asilomar Conf. Signal Syst. Comput.*, Nov. 2009, pp. 605–609.
- [6] K. Tu, T. M. Duman, M. Stojanovic, and J. G. Proakis, "Multiple-resampling receiver design for OFDM over Doppler-distorted underwater acoustic channels," *IEEE J. Ocean. Eng.*, vol. 38, no. 2, pp. 333–346, Apr. 2013.
- [7] B. Li, J. Huang, S. Zhou, K. Ball, M. Stojanovic, L. Freitag, and P. Willett, "MIMO-OFDM for high-rate underwater acoustic communications," *IEEE J. Ocean. Eng.*, vol. 34, no. 4, pp. 643–644, Oct. 2009.
- [8] S. Lu and N. Al-Dhahir, "Coherent and differential ICI cancellation for mobile OFDM with application to DVB-H," *IEEE Trans. Wireless Commun.*, vol. 7, no. 11, pt. 1, pp. 4110–4116, Nov. 2008.
- [9] Y. M. Aval and M. Stojanovic, "Fractional FFT demodulation for differentially coherent detection of acoustic OFDM signals," in *Proc. 46th Asilomar Conf. Signal Syst. Comput.*, Nov. 2012, pp. 1525–1529.

- [10] S. Yerramalli, M. Stojanovic, and U. Mitra, "Partial FFT demodulation: A detection method for highly Doppler distorted OFDM systems," *IEEE Trans. Signal Process.*, vol. 60, no. 11, pp. 5906–5918, Nov. 2012.
- [11] M. Stojanovic, "A method for differentially coherent detection of OFDM signals on Doppler-distorted channels," in *Proc. IEEE Sensor Array Multichannel Signal Process. Workshop*, Oct. 2010, pp. 85–88.
- [12] Y. M. Aval and M. Stojanovic, "A method for differentially coherent multichannel processing of acoustic OFDM signals," in *Proc. 7th IEEE Sensor Array Multichannel Signal Process. Workshop*, Jun. 2012, pp. 73–76.
- [13] B. Muquet, W. Zhengdao, G. Giannakis, M. D. Courville, and P. Duhamel, "Cyclic prefixing or zero padding for wireless multicarrier transmissions?," *IEEE Trans. Commun.*, vol. 50, no. 12, pp. 2136–2148, Dec. 2002.
- [14] Z. Wang, S. Zhou, G. B. Giannakis, C. R. Berger, and J. Huang, "Frequency-domain oversampling for zero-padded OFDM in underwater acoustic communications," *IEEE J. Ocean. Eng.*, vol. 37, no. 1, pp. 14–24, Jan. 2012.
- [15] X. Wang and K. Liu, "An adaptive channel estimation algorithm using time-frequency polynomial model for OFDM with fading multipath channels," *EURASIP J. Appl. Signal Process.*, vol. 2002, no. 1, pp. 818–830, Aug. 2002.
- [16] T. Wang, J. G. Proakis, and J. R. Zeidler, "Techniques for suppression of intercarrier interference in OFDM systems," in *Proc. IEEE Wireless Commun. Netw. Conf.*, Mar. 2005, vol. 1, pp. 39–44.
- [17] Y. M. Aval and M. Stojanovic, "Multi-FFT demodulators," 2014 [Online]. Available: <http://millitsa.coe.neu.edu/?q=projects>
- [18] J. C. Peterson and M. B. Porter, "Virtual timeseries experiment (VirTEX)—Quick start," 2011 [Online]. Available: <http://oalib.hlsresearch.com/Rays/VirTEX/README.pdf>
- [19] M. B. Porter, "The BELLHOP manual and user's guide: Preliminary draft," 2011 [Online]. Available: <http://oalib.hlsresearch.com/Rays/HLS-2010-1.pdf>
- [20] E. V. Zorita and M. Stojanovic, "Space-frequency coded OFDM for underwater acoustic communications," in *Proc. IEEE OCEANS Conf.*, Virginia Beach, VA, USA, Oct. 2012, DOI: 10.1109/OCEANS.2012.6404916.

- [21] W. E. Ryan and S. Lin, *Channel Codes: Classical and Modern*. Cambridge, U.K.: Cambridge Univ. Press, 2009, ch. 5.



**Yashar M. Aval** (S'11) graduated from the University of Tehran, Tehran, Iran, in 2002 and received the M.S. degree in electrical engineering from Sharif University of Technology, Tehran, Iran, in 2005. Currently, he is working toward the Ph.D. degree in electrical engineering at Northeastern University, Boston, MA, USA.

His research interests include digital communications, OFDM, underwater acoustic communications, and underwater acoustic networks.



**Milica Stojanovic** (SM'08–F'10) graduated from the University of Belgrade, Belgrade, Serbia, in 1988 and received the M.S. and Ph.D. degrees in electrical engineering from Northeastern University, Boston, MA, USA, in 1991 and 1993, respectively.

She was a Principal Scientist at the Massachusetts Institute of Technology (MIT), Cambridge, MA, USA, and in 2008, she joined Northeastern University where she is currently a Professor of Electrical and Computer Engineering. She is also a Guest Investigator at the Woods Hole Oceanographic Institution, Woods Hole, MA, USA, and a Visiting Scientist at MIT. Her research interests include digital communications theory, statistical signal processing and wireless networks, and their applications to underwater acoustic systems.

Prof. Stojanovic is an Associate Editor for the IEEE JOURNAL OF OCEANIC ENGINEERING and a past Associate Editor for the IEEE TRANSACTIONS ON SIGNAL PROCESSING and the IEEE TRANSACTIONS ON VEHICULAR TECHNOLOGY. She also serves on the Advisory Board of the IEEE COMMUNICATION LETTERS, and chairs the IEEE Ocean Engineering Society's Technical Committee for Underwater Communication, Navigation, and Positioning.